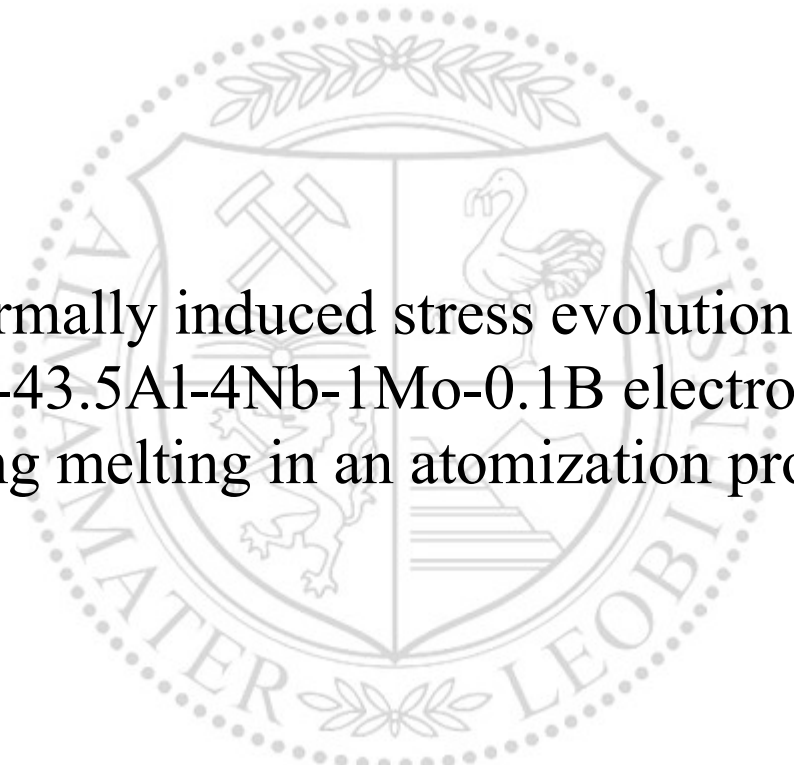Chair of Mechanics

Master's Thesis

Thermally induced stress evolution in a Ti-43.5Al-4Nb-1Mo-0.1B electrode during melting in an atomization process

Jakob Bialowas, BSc

March 2019

EIDESSTATTLICHE ERKLÄRUNG

Ich erkläre an Eides statt, dass ich diese Arbeit selbständig verfasst, andere als die angegebenen Quellen und Hilfsmittel nicht benutzt, und mich auch sonst keiner unerlaubten Hilfsmittel bedient habe.

Ich erkläre, dass ich die Richtlinien des Senats der Montanuniversität Leoben zu "Gute wissenschaftliche Praxis" gelesen, verstanden und befolgt habe.

Weiters erkläre ich, dass die elektronische und gedruckte Version der eingereichten wissenschaftlichen Abschlussarbeit formal und inhaltlich identisch sind.

Datum 01.03.2019

Unterschrift Verfasser/in
Jakob, Bialowas
Matrikelnummer: 00735352

Acknowledgements

Kurzfassung

Die Legierung Ti-43.5Al-4Nb-1Mo-0.1B, bekannt unter dem Markennamen TNM, ist ein Leichtbauwerkstoff, welcher für hochbeanspruchte Bauteile entwickelt wurde, die hohen Einsatztemperaturen ausgesetzt werden. Mit einer Dichte von $3.9\,\mathrm{g/cm^3}$ und hoher Festigkeit auch bei Temperaturen über 700°C eignet sich dieser Werkstoff ideal für den Einsatz in der Flugzeugindustrie. TNM kommt bereits als Material der Turbinenschaufeln in der Niederdruckstufe der Geared Turbo Fan (GTF) Turbine im Flugzeugbau zum Einsatz.

Die Fertigung dieser Bauteile erfolgt mithilfe von pulvermetallurgischen Verfahren, wobei das Pulver im sogenannten EIGA-Verfahren (Electrode Induction melting Gas Atomisation) hergestellt wird. Dabei wird eine TNM Elektrode kontinuierlich durch induktiv erzeugten Wärmeeintrag abgeschmolzen, und die Schmelze anschließend verdüst. Für die Optimierung dieses Prozesses ist die genaue Kenntnis des zeitlich veränderlichen Temperatur- und Spannungsfeldes in der Elektrode maßgeblich. Eine experimentelle Charakterisierung ist jedoch zu komplex, daher wird in dieser Arbeit der Prozess mithilfe eines nummerischen Modells abgebildet.

Dazu müssen drei Phasen der Herstellung modelliert werden: (i) zunächst wird die Elektrode aus dem Schleuderguss abgekühlt, wobei sich hier schon aufgrund der auftretenden Temperaturgradienten Eigenspannungen einstellen. (ii) Danach erfolgt das Aufheizen der Elektrode bis Schmelztemperatur durch eine Wärmequellenverteilung, wie sie aufgrund der Anordnung der Induktionsspulen zu erwarten ist. Diese Wärmequellen wandern zeitlich gesteuert, entsprechend der Geschwindigkeit des Abschmelzprozesses die Elektrode entlang. (iii) Zufolge dieser Temperaturhistorie ergeben sich thermomechanische Spannungen, die den in Phase (i) entstandenen überlagert werden.

Die komplexe Temperaturgeschichte in Phase (ii) kann mit den Standardmöglichkeiten kommerzieller Finite Elemente Software nicht aufgebracht werden, sondern muss über zusätzliche User-Subroutines programmiert werden.

Dieses Modell erlaubt es, die resultierenden Spannungen für unterschiedliche Geometrien und Spulenanordnungen zu ermitteln. Aus der Zielsetzung, die auftretenden Spannungsmaxima zu minimieren, können Richtlinien für die Wahl optimaler Prozess- und Geometrieparameter abgeleitet werden.

Abstract

The alloy Ti-43.5Al-4Nb-1Mo-0.1B, known by the brand name TNM, is a material for light weight constructions. It is designed for heavy-duty components, that are used at elevated operation temperatures. With a density of $3.9\,\mathrm{g/cm^3}$ and high strength even at temperatures over 700°C this material is suitable for applications in aviation industry. TNM is used as a material for turbine blades of the low pressure stage of the geared turbo fan (GTF) turbine in aircraft.

These components are produced by powder metallurgy processes. The powder is manufactured in a process called EIGA (Electrode Induction melting Gas Atomisation), where a TNM electrode is melted continuously by means of inductively generated heat. Subsequently the liquefied material is atomised through a nozzle. The optimisation of this process requires the knowledge of the time varying temperature and stress field of the electrode. An experimental characterisation is too complex, therefore a numerical model to represent this process is presented.

For this purpose three manufacturing phases have to be modelled: (i) initially a centrifugal cast electrode cools down and residual stresses appear due to temperature gradients. (ii) Subsequently the electrode is heated up until melting, where the heat source distribution is determined by the arrangement of the induction coils. These heat sources move controlled by time with the velocity of the melting process along the electrode. (iii) Thermo-mechanical stresses occur due to the resulting temperature field and are superimposed with the stresses calculated in phase (i).

The complex temperature fields in phase (ii) cannot be modelled with the standard functionality of commercially available finite element software. To accomplish this additional user-subroutines have to be coded.

This model allows to determine the stress field for variable geometries and arrangements of the induction coils. Given the objective to minimise the maximal occurring stresses, guidelines for the optimal choice of geometry and process parameters can be deduced.

Contents

List of Symbols

Symbol	Unit	Description
1	$[m]$	first global coordinate
2	$[m]$	second global coordinate
a_{df}	$[-]$	coefficient of exponential function of additional heat flux
α	$[-]$	α-phase
α_2	$[-]$	disordered α-phase
α	$[K^{-1}]$	thermal expansion coefficient
α_k	$[\frac{W}{m^2 K}]$	convective heat coefficient
b_{df}	$[-]$	coefficient of exponential function of additional heat flux
β	$[-]$	β-phase
β	$[K^{-1}]$	coefficient of expansion
c_{df}	$[-]$	coefficient of exponential function of additional heat flux
c_p	$[\frac{J}{kgK}]$	specific heat capacity
D_{cyl}	$[m]$	diameter of a cylinder
ε	$[-]$	emissivity
ε_{eq}^p	$[-]$	equivalent plastic strain
η	$[\frac{kg}{ms}]$	dynamic viscosity
$f_1(Pr)$	$[-]$	function dependent on the Prandtl number
$f_3(Pr)$	$[-]$	function dependent on the Prandtl number
g	$[\frac{m}{s^2}]$	gravitational acceleration
γ	$[-]$	γ-phase
h_{cyl}	$[m]$	height of a cylinder
$\boldsymbol{I}$	$[-]$	identity matrix
κ	$[\frac{m^2}{s}]$	thermal diffusivity
L	$[-]$	liquid-phase
λ	$[\frac{W}{mK}]$	thermal conductivity
$\boldsymbol{\lambda}$	$[\frac{W}{mK}]$	conductivity matrix
L	$[m]$	characteristic length
Nu	$[-]$	Nusselt number
ν	$[\frac{m^2}{s}]$	kinematic viscosity

Symbol	Unit	Description
$Nu_{cylvert}$	$[-]$	Nusselt number for a cylindrical vertical surface
Nu_{cylhor}	$[-]$	Nusselt number for a cylindrical horizontal surface
ϕ_q	$[\frac{W}{m^2}]$	heat flux
$\boldsymbol{\phi_q}$	$[\frac{W}{m^2}]$	heat flux vector
Pr	$[-]$	Prandtl number
Q_{amp}	$[-]$	multiplicative factor of the heat flux distibution in DFLUX subroutine
q_{df}	$[-]$	heat flux calculated in DFLUX subroutine
r	$[m]$	first coordinate of an axially symmetric model
Ra	$[-]$	Rayleigh number
ρ	$[\frac{kg}{m^3}]$	mass density
R_S	$[\frac{J}{kgK}]$	specific gas constant
σ	$[\frac{W}{m^2K^4}]$	Stefan-Boltzmann-constant
σ_{max}	$[\frac{N}{mm^2}]$	maximum pricipal stress
σ_{Mises}	$[\frac{N}{mm^2}]$	mises stress
σ_z	$[\frac{N}{mm^2}]$	stress component in z-direction
T_∞	$[K]$	ambient temperature
ΔT	$[K]$	temperature difference
T	$[K]$	temperature
T_{eu}	$[K]$	eutectoid temperature
T_F	$[K]$	temperature of the fluid
$T_{\gamma,solv}$	$[K]$	γ-solvus temperature
T_m	$[K]$	melting temperature
T_S	$[K]$	surface temperature
T_*	$[K]$	reference temperature
T_W	$[K]$	temperature of the wall
u_r	$[m]$	first degree of freedom
u_z	$[m]$	second degree of freedom
z	$[m]$	second coordinate of an axially symmetric model
z_{coil}	$[m]$	current position of the induction coil relative to the z-coordinate

List of Abbreviations

2D	two dimensional
3D	three dimensional
AC	alternating electric current
Al	aluminium
AM	additive manufacturing
approx.	approximately
Ar	argon
at%	atomic percent
ATR	Alumino-Thermic Reduction
B	boron
bcc	body-centered cubic
BDTT	brittle to ductile transition temperature
C	carbon
CAD	computer-aided design
CAE	Complete Abaqus Environment
Cu	copper
DC	direct electric current
EIGA	Electrode Induction melting Gas Atomization
EM	electromagnetic
Fe	iron
FEM	finite element method
GTF^{TM}	Geared Turbofan^{TM}
GUI	graphical user interface
He	helium
HIP	Hot Isostatic Pressing
IM	ingot metallurgy
inp.	input
ISM	Induction Skull Melting
IWM	Institut für Metallkunde und Metallische Werkstoffe
LPT	low pressure turbine
Mo	molybdenum

N	nitrogen
Nb	niobium
Ni	nickel
O	oxygen
PAM	Plasma Arc Melting
PIGA	Plasma melting Inert Gas Atomization
PM	powder metallurgy
RT	room temperature
Ti	titanium
TiAl	titanium aluminides
TIP	thermally induced porosity
TNM	titanium aluminide with content of niobium and molybdenum
US	User Subroutine
VAR	Vacuum Arc Melting/Remelting
VIM	Vacuum Induction Melting

1 Introduction

In an era of limited raw materials and resources, demands on energy efficiency are growing. With continuously increasing worldwide mobility the aviation industry has a great responsibility in terms of climate protection and sustainable use of limited natural resources. A variety of programs have been launched in order to substantially reduce emissions of passenger planes, see Mayer et al. (2017). In order to decrease fuel consumption, CO_2, NO_x and noise emissions new structural materials have to withstand extreme conditions. The use of β-solidifying γ-titanium aluminides (TiAl) based alloys of the 3rd generation, so-called TNM alloys (titanium aluminide with content of niobium and molybdenum (TNM)) is one approach to meet these goals, see Clemens and Mayer (2013, 2016), Mayer et al. (2017). With a density of 3.8-$4.1\,g/cm^3$ TNM is an excellent material for the use in advanced high-performance combustion engines, see Schwaighofer et al. (2014a).

One particular application for TNM are blades of the last low pressure turbine (LPT) stage of the new Geared Turbofan^{TM} (GTF^{TM}) engine. These blades currently replace nickel (Ni)-based alloys with a density of approximately (approx.) $8\,g/cm^3$ and have the potential to replace even more stages of the GTF^{TM} engine, see Mayer et al. (2017). A sectional view of a GTF^{TM} engine is shown in Figure 1.1. The turbine blades of the LPT stage are coloured blue in this figure.

TNM is a high tech material that perfectly meets the goals that are necessary for the usage in aviation industry. However manufacturing of TiAl based turbine blades requires multiple steps and specific know-how. From all the possible manufacturing and processing routes the powder metallurgy (PM) route provides the highest homogeneity within the semi manufactured products and hence the best option for further process steps.

1.1 Motivation

The production of metal powders is an expensive process that depends on a variety of dependent and independent factors. One possible route of PM is the continuous
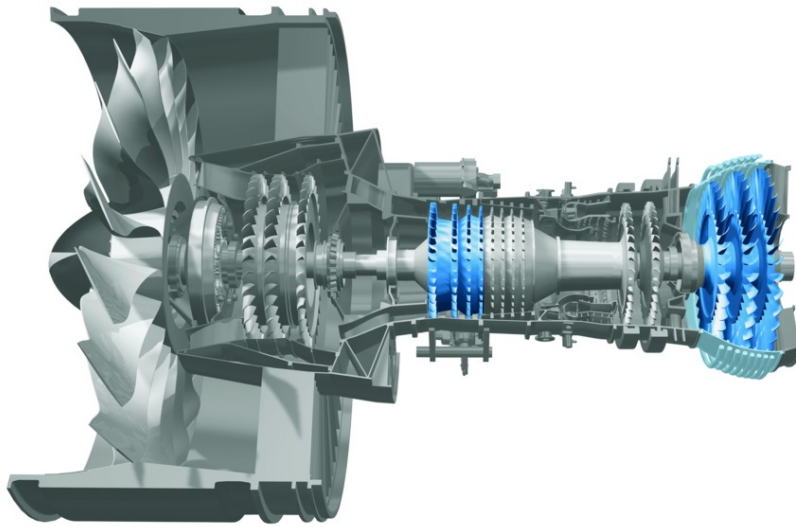
Figure 1.1: Geared turbofan. Image courtesy of MTU Aero Engines (2018).

melting of a cylindrical ingot and subsequent atomization of the liquid metal. To use this route in an industrial scale it is necessary to increase the diameters of the ingots and the speed of melting. Since plants for such a process are not versatile and adaptability for multiple geometries and materials is time-consuming and cost-intensive a trial-and-error method is not an option from an economic point of view.

1.2 Goals

The main goal of this thesis is to set up a versatile model with the finite element method (FEM) to test multiple configurations of geometry and arrangements of heating devices. Such a simulation is a first step in finding the ideal configuration for continuous melting processes. It will also provide an insight into the mechanical and thermal behaviour of the material during the process. With this information it will be possible to eliminate influencing factors that would cause problems within the production line in the future by identifying the reasons for damage.

2 Fundamentals

This chapter will provide basic information on the material TNM, manufacturing details and the most important characteristics of its physical behaviour. Furthermore it will recapitulate the mechanisms of heat transfer relevant for the current work. Finally this chapter closes with various possibilities of heat induction in TNM and established routes of atomization of melted metal.

2.1 TNM

TNM is a β-solidifying γ-TiAl based alloy of the third generation. The name TNM traces back to the elements niobium (Nb) and molybdenum (Mo). These elements have the function of stabilizing the β-phase throughout the solidification of the material. The comparatively high volume fraction of β-phase has advantageous effects on the hot-deformation behaviour of TNM, which is essential for manufacturing heavy-duty parts. The nominal composition in atomic percent (at%) is Ti-43.5Al-4Nb-1Mo-0.1B. The experimental quasi-binary section of the TNM alloy system is shown in Figure 2.1. The phase fraction diagram of Figure 2.1 shows that multiple phase transformations occur within a narrow temperature range. With suitable thermo-mechanical processing it is possible to reach strength-levels above $1000\,\mathrm{MPa}$ at room temperature (RT), see Mayer et al. (2017). Additional advantages of intermetallic γ-TiAl based alloys are high specific stiffness, good oxidation resistance, resistance against "titanium fire" and good creep properties up to high temperatures. A comparison of the specific Young's modulus of γ-TiAl based alloys and Ni-based superalloys, that are currently used for heavy-duty parts is shown in Figure 2.2. Figure 2.3 shows variations of the specific yield strength with temperature for multiple structural materials at which the upper strength limit of advanced titanium aluminides is represented by forged and heat treated TNM, see Clemens and Mayer (2013).

In general, advanced intermetallic γ-TiAl based alloys, such as TNM can be processed via multiple routes. Established routes on the industrial scale are ingot metallurgy (IM), PM and casting. Additive manufacturing (AM) of TNM and similar materials
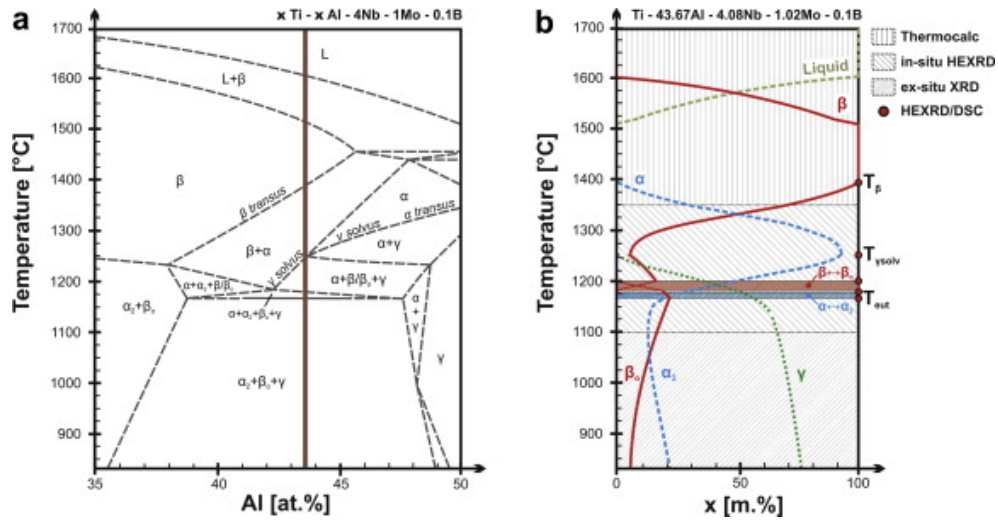
Figure 2.1: Experimental quasi-binary section of the TNM alloy system, where the nominal Al-content if the TNM alloy is indicated as a vertical line, together with the experimentally determined phase fraction diagram of a Ti-43.67Al-4.08Nb-1.02Mo-0.1B (in at%) alloy. Figure and caption taken from Schwaighofer et al. (2014b), fig 1, with permission from Elsevier.
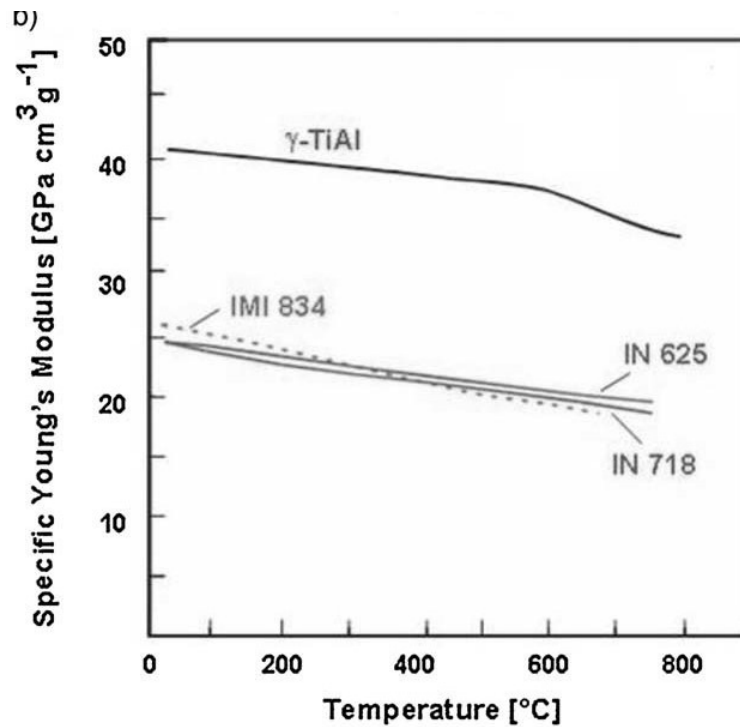
Figure 2.2: Variation of specific Young's modulus with temperature of selected structural materials in comparison with intermetallic γ-TiAl based alloy. IMI 834=titanium alloy, IN 625 and IN 718=nickel basis super alloys. Figure and caption taken from Clemens and Mayer (2013), fig 1b, with permission from Wiley-VCH.

Figure 2.3: Variation of specific Yield Strength with temperature of selected structural materials in comparison with intermetallic γ-TiAl based alloy. Figure and caption taken from Appel et al. (2016), fig 1a, with permission from Elsevier.

is still the subject of research but on the verge of a breakthrough to be used on an industrial scale. Since the needs of the industry for complex components and innovative high-temperature materials are growing, AM will provide solutions where the limits of conventional processing are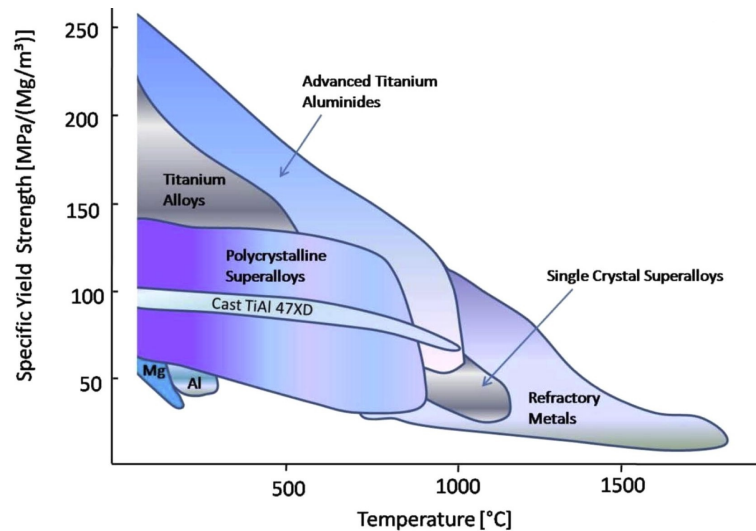 exceeded. Figure 2.4 shows details for the above mentioned manufacturing and processing routes, see Balla et al. (2016), Mayer et al. (2017).

2.1.1 Design of TNM

The first commercial application of γ-TiAl based alloys was announced in 1999. Since then the design of this material evolved towards an economic feasibility of wrought processing. The main goal was to create a material that will provide the necessary physical properties and can be processed near conventionally. For the design concept of TNM it is important to be able to perform forging and rolling operations for small parts on an industrial scale. For this secondary forming operations a fine-grained and isotropic microstructure is needed. Furthermore the material must not only withstand variations within the processing routes but also variations in the chemical composition with little to no changes in physical and microstructural properties. Since the parts are exposed to service temperatures in the range of 600-750 °C over long terms the parts must also show resistance on microstructural and geometrical changes. Finally the material must satisfy certain requirements concerning machinability with different
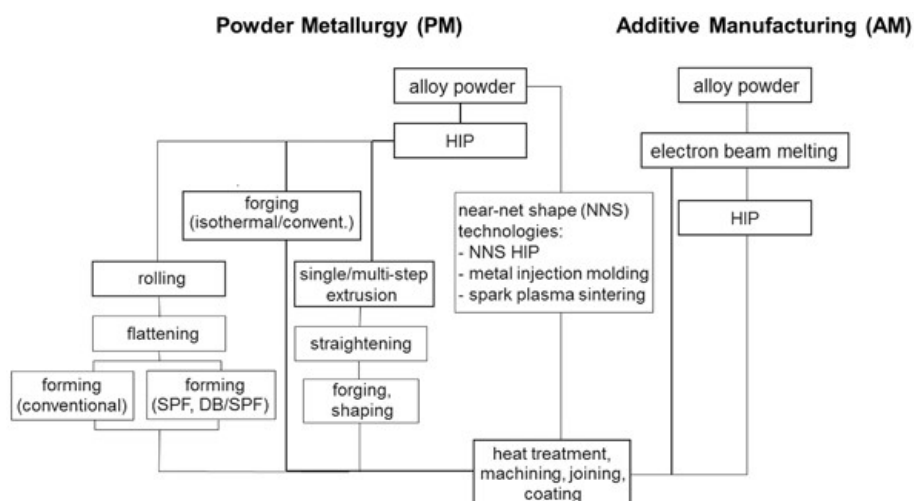
Figure 2.4: Manufacturing and processing routes in use for engineering γ-TiAl based alloys. Figure and caption taken from Clemens and Mayer (2015), fig 3, with permission from Springer-Verlag Wien.

techniques like turning or mechanical and chemical milling, see Schloffer et al. (2012), Clemens and Mayer (2013), Mayer et al. (2017).

Clemens et al. (2008) formulated the following six specifications:

- *To avoid casting texture after solidification it is necessary to obtain a refined equiaxed microstructure.*

- *The solidification path via L$\to$ L+$\beta$$\to$$\beta$$\to$ ... should be achieved instead of a peritectic solidification via L$\to$ L+$\beta$$\to$$\alpha$$\to$ ... to ensure an intrinsic grain refinement.*

- *A significant volume fraction of distorted body-centered cubic (bcc) β-phase will help to provide a sufficient number of slip systems and improve deformability at elevated temperatures*

- *A single α-phase at forging and heat treatment temperatures should be avoided to counteract grain coarsening.*

- *For reproducible heat treatments the ratio of γ-TiAl, α_2-Ti$_3$Al and β_0-phase should be well-balanced.*

- *The decomposition of the ordered β_0-phase into ω-phase should be avoided to counteract embrittlement.*

Using multiple software packages Clemens et al. (2008) designed a γ-TiAl that featured all necessary properties and was named TNM$^{\text{TM}}$, see Clemens and Mayer (2013).

2.1.2 Hot Working Behaviour of TNM

One of the main goals for the design of TNM^{TM} was to improve the hot-workability of γ-TiAl based alloys, which is conducted exclusively above the brittle to ductile transition temperature (BDTT) of 700 °C, see Clemens and Mayer (2016). This particular alloy solidifies via the β-phase. Moreover it features an adjustable β/B2-phase volume fraction as described in Wallgram et al. (2009). Hot die forging under near conventional conditions is possible due to the high volume fractions of β-phase at elevated temperatures. The improved deformability of the material can be traced back to an increased number of slip systems provided by a β-phase with bcc lattice. To stabilize the β-phase by extending the β-phase field region to higher aluminium (Al) contents both Nb and Mo are used as alloying elements. The stabilizing effect of Mo compared to Nb is four times stronger. In addition these two alloying elements move the melting temperature T_m and the eutectoid temperature T_{eu} to higher temperatures. Thus, the $T_{\gamma,solv}$ is set to the Al-rich side, that improves the refinement of the microstructure. Nb and Mo decelerate thermally activated dislocation climbing by raising the activation energy of diffusion in both γ-TiAl and α_2-Ti$_3$Al. Thereby an increase in creep resistance and high-temperature strength can be realized. Boron (B) is used to secure grain refinement during solidification and additionally to counteract grain coarsening during subsequent heat treatments by forming very stable borides. The β-phase and its ordered counterpart B2 decompose into phases with lower crystal symmetry, that are brittle. This decomposition is time-dependent and influenced by the content of Al and other elements. Thus, this effect has to be taken into account while processing along various routes, see Wallgram et al. (2009), Mayer et al. (2017), Clemens et al. (2008). The β-phase is needed to improve deformability at elevated temperatures, but these properties are not desired in components that are used at service temperatures in a range of 700-800 °C. Therefore the volume fraction of the β-phase should be reduced to a minimum to prevent a decline in creep resistance, see Schloffer et al. (2012).

2.2 Heat Transfer

Verein Deutscher Ingenieure, VDI (2013) define heat as form of energy, that transfers from a system to its surrounding solely due to a difference in temperature. This transport of energy is called heat transfer and occurs, as stated by the second law of thermodynamics, along a temperature gradient in direction of decreasing tempera-

ture. In general literature differentiates heat transfer between material bound transfer, called conduction and convection, and not material bound transfer, called radiation.

2.2.1 Heat Transfer by Conduction

Microscopic collisions and movement of particles including molecules, atoms and electrons, cause a transfer of kinetic and potential energy, also known as internal energy. Conduction occurs in solids, liquids and gases independently from the macroscopic movement of the material. If there is a temperature gradient $\partial T/\partial x$ in direction of x, the heat flux, which is heat transfer per unit of area and unit of time, is solely dependent on a material constant called thermal conductivity λ. This material constant can be dependent on temperature and direction and is defined to be positive. J.B.J. Fourier[1] formulated a law of heat conduction, also known as Fourier's law, that states the time rate of heat transfer through a material is proportional to the negative gradient in the temperature and to the area, at right angles to that gradient, through which the heat flows. The three dimensional (3D) formulation of the heat transfer by conduction, that is used for solving heat transfer problems with the FEM is governed by equation 2.1, with $\boldsymbol{\phi_q}$ in W/m^2 as the heat flux vector and $\boldsymbol{\lambda}$ in W/mK as the conductivity matrix. With $\boldsymbol{\lambda}$ being a matrix, it is possible to model anisotropic material behaviour. For most materials it is valid to assume isotropic conductivity, so that $\boldsymbol{\lambda} = \lambda \boldsymbol{I}$, where λ is a scalar and $\boldsymbol{I}$ is the identity matrix, see VDI (2013), Abaqus-Documentation (2018).

$$\boldsymbol{\phi_q} = -\boldsymbol{\lambda} \; grad \; T(x,y,z) \tag{2.1}$$

2.2.2 Heat Transfer by Convection

Convection is defined as heat transfer due to the movement of particles within a fluid. This movement leads to a transport of enthalpy and kinetic energy. Thus, this form of heat transfer is not only dependent on material properties but also on the process itself. The heat transfer between a solid body and a fluid is called convective heat transmission. It is specified by Newton's cooling law that was formulated by I. Newton[2] and can be described by equation 2.2, where α_k is the heat transfer

---

[1] Jean-Baptiste Joseph Fourier (21 March 1768 – 16 May 1830): French mathematician and physicist
[2] Sir Isaac Newton (4 January 1643 - 31 March 1727): English mathematician, physicist, astronomer, theologian and author

coefficient in W/m^2K, T_W is the temperature of the wall (solid body) and T_F the temperature of the fluid.

$$\phi_q = -\alpha_k \cdot (T_W - T_F) \tag{2.2}$$

The heat flux of convection strongly depends on the profile of the temperature and velocity field. Therefore displaying this process is a complex task, especially for turbulent flow. To simplify these relations all influences are condensed in the heat transfer coefficient α_k, that depends on the process itself (velocity, turbulence, temperature and orientation of the flow), the geometry of the solid body as well as its surface roughness. For practical usage empirical correlations were derived for multiple applications and enable simple calculations of α_k.

The calculation method and the material values to calculate α_k are taken from VDI (2013), Marek and Nitsche (2012). J. V. Boussinesq [1] developed a simplification of the temperature dependency of thermophysical material values in the Navier [2]-Stokes [3]-equation. This simplification called Boussinesq-approximation is only valid for small temperature differences ΔT. If the constrain of a small ΔT is not met VDI (2013) considers it correct to calculate the heat flux by convection with approximated temperature dependent material values. In this case a reference temperature T_* is used for the calculation and is governed by equation 2.3, with the surface temperature T_S and the ambient temperature T_∞.

$$T_* = \frac{1}{2}(T_S + T_\infty) \tag{2.3}$$

Dimensionless numbers provide a clear representation of physically similar conditions and allow to compare these conditions. For the heat transfer by convection the Nusselt number Nu is a dimensionless number, that is necessary to calculate a temperature dependent α_k. It is named after E. Nußelt [4] and is governed by equation 2.4, with λ as thermal conductivity and L as characteristic length.

$$Nu = \frac{\alpha_k L}{\lambda} \tag{2.4}$$

---

[1] Joseph Valentin Boussinesq (13 March 1842 – 19 February 1929): French mathematician and physicist

[2] Claude-Louis Navier (10 February 1785 – 21 August 1836): French engineer and physicist

[3] Sir George Gabriel Stokes (13 August 1819 – 1 February 1903): Anglo-Irish physicist and mathematician

[4] Ernst Kraft Wilhelm Nußelt (25 November 1882 - 1 September 1957): German engineer

The Nusselt number is also a function of the dimensionless numbers Prandtl and Rayleigh, named after L. Prandtl [1] and Lord Rayleigh [2]. For a vertical flat surface the governing equations are 2.5 and 2.6, with $f_1(Pr)$ as a function of the Prandtl number Pr and Ra as Rayleigh number.

$$Nu_{flat} = \left\{ 0.825 + 0.387 \left[Ra \cdot f_1(Pr) \right]^{\frac{1}{6}} \right\}^2 \tag{2.5}$$

$$f_1(Pr) = \left[1 + \left(\frac{0.492}{Pr} \right)^{9/16} \right]^{-16/9} \tag{2.6}$$

To calculate the Nusselt number for other geometries relative to the flow direction the results of equation 2.5 are used in an extended equation. The Nusselt number for the surface of a vertical cylinder $Nu_{cylvert}$ is governed by equation 2.7, with h_{cyl} as the height and D_{cyl} as diameter of the cylinder.

$$Nu_{cylvert} = Nu_{flat} + 0.435 \frac{h_{cyl}}{D_{cyl}} \tag{2.7}$$

For flat horizontal geometries heat transfer by convection differentiates between the loss of heat on the top and bottom of the cylinder. For horizontal flow this distinction is not relevant and the Nusselt number for a horizontal cylindrical surface Nu_{cylhor} can be calculated with equation 2.8. In this case the function of the Prandtl number $f_3(Pr)$ is governed by equation 2.9. The characteristic length L in equation 2.4 changes to half of the circumference, as described in equation 2.10.

$$Nu_{cylhor} = \left\{ 0.752 + 0.387 \left[Ra \cdot f_3(Pr) \right]^{1/6} \right\}^2 \tag{2.8}$$

$$f_3(Pr) = \left[1 + \left(\frac{0.559}{Pr} \right)^{9/16} \right]^{-16/9} \tag{2.9}$$

$$L = \frac{\pi}{2} \cdot d \tag{2.10}$$

The Rayleigh number in equations 2.5 and 2.8 characterizes the heat transfer within a fluid. If Ra exceeds a critical value, the heat transfer is governed by convection. Below this value the heat transfer is governed by conduction. Equation 2.11 describes the relationship between Ra, the isobaric coefficient of expansion β, the gravitational

---

[1] Ludwig Prandlt (4 February 1875 − 15 August 1953): German engineer
[2] John William Strutt, Lord Rayleigh (12 November 1842 − 30 June 1919): British physicist

acceleration g, the kinematic viscosity ν, the characteristic length L, the thermal diffusivity κ, T_∞ and T_*.

$$Ra = \frac{g \; \beta \; L^3}{\kappa \; \nu}(T_* - T_\infty) \tag{2.11}$$

The Prandtl number, that is necessary to calculate equation 2.6 is governed by equation 2.12. It is a temperature and pressure dependent material constant.

$$Pr = \frac{\nu}{\kappa} \tag{2.12}$$

The thermal diffusivity κ is a material property, that describes the time dependent spatial distribution of the temperature due to the heat flux generated by a temperature gradient. It is governed by equation 2.13, where λ is the thermal conductivity, ρ the density and c_p the specific heat capacity.

$$\kappa = \frac{\lambda}{\rho \; c_p} \tag{2.13}$$

The kinematic viscosity ν in 2.12 and 2.11 is a measurement for the resistance of a fluid for shear stresses. It is closely detained from the dynamic viscosity η by dividing by the density ρ, as presented in equation 2.14.

$$\nu = \frac{\eta}{\rho} \tag{2.14}$$

The density of an ideal gas is pressure and temperature dependent as described in equation 2.15, where R_S is the specific gas constant with a value of 287.058 $^J/_{kgK}$.

$$\rho = \frac{p}{R_S \; T_*} \tag{2.15}$$

To calculate the temperature dependent heat transfer coefficient α_k, firstly the input parameters from equations 2.13 to 2.15 have to be calculated for the surrounding fluid. The calculation of the dimensionless numbers from equations 2.5 to 2.12 are executed by means of the previously calculated parameters. With the right choice of the equation for the Nusselt number it is possible to calculate the temperature and geometry dependent α_k.

2.2.3 Heat Transfer by Radiation

Every body emits energy through electromagnetic (EM) waves to its surrounding. A more precise definition is that every body with a temperature $T > 0\ K$ emits heat to its surrounding, but since the third law of thermodynamics states that there is no body with a temperature $T \leq 0\ K$ the first definition is sufficient. This emission of radiation occurs because internal energy converts into an EM wave that transports the energy. The emission of heat radiation has an upper limit, that is dependent on the temperature of the body and is described by the equation 2.16. J. Stefan [1] published this principle that was deduced by his student L. Boltzmann [2] by means of the second law of thermodynamics. The Stefan-Boltzmann constant, denoted by σ is a constant of proportionality in equation 2.16 and has the value $(5.670400 \pm 0.00004) \cdot 10^{-8} \frac{W}{m^2 K^4}$, see Stephan (2008), VDI (2013).

$$\phi_q = \sigma T^4 \qquad (2.16)$$

An emitter producing this maximum possible heat flux, as described by equation 2.16 is called black body. To describe radiation of a real body a correction factor ε is introduced to equation 2.17, called emissivity which depends also on surface properties like e.g. surface roughness, see Stephan (2008).

$$\phi_q = \varepsilon \sigma T^4 \qquad (2.17)$$

2.3 Finite Element Method

The Finite Element Method is a general purpose numerical method to solve physical or engineering boundary value problems. It transposes this boundary value problem with a continuous solution into an algebraic system of equations with discrete solutions. To be able to perform this discretization shape functions are used that are applicable for one element only.

---

[1] Josef Stefan (24 March 1835 − 7 January 1893): Carinthian Slovene physicist, mathematician and poet

[2] Ludwig Eduard Boltzmann (February 20 1844 − September 5 1906): Austrian physicist and philosopher

2.3.1 Heat Transfer

The equation of thermal equilibrium has to be solved in order to calculate the temperature at a given point of the model. The boundary conditions for a heat transfer problem are:

- definition of temperature T at some part of the surface, which is a Dirichlet[1] boundary condition

- definition of the heat flux ϕ_q entering the domain across the surface, which is a Neumann[2] boundary condition

- definition of the heat flux ϕ_q by convection and/or radiation

2.3.2 Mechanical Stresses

The goal of a mechanical analysis is to obtain a set of algebraic equations to solve for the unknown quantities, i.e. displacements, stresses and strains. Equivalent to the heat transfer problem boundary conditions have to be defined for the mechanical problem:

- Dirichlet boundary condition: definition of the displacement at a certain point

- Neumann boundary condition: definition of forces or stresses at a certain point

2.3.3 Uncoupled Analysis

It is important to note, that for the calculations performed in this thesis the heat transfer problem is uncoupled from the mechanical problem, i.e. the solutions of the mechanical calculation do not influence the heat transfer problem. The solution of the heat transfer problem can be applied as a thermal load in a subsequent mechanical analysis.

The following section 2.4 describes the various possibilities to insert heat into components made of TNM.

---

[1]Peter Gustav Lejeune Dirichlet (13 February 1805 − 5 May 1859): German mathematician
[2]Carl Gottfried Neumann (7 May 1832 − 27 March 1925): German mathematician

2.4 Heat Input in TNM

This section describes various methods of heat input in parts made of TNM. Firstly the process of ingot production is described. In the following subsections the subsequent manufacturing of these ingots is explained, with insights in atomization and melting processes. In this thesis the main focus lies on the unidirectional heat input used for melting of semi-finished products.

2.4.1 Ingot Production

Ingots are semi-finished products made of relatively pure material. This material, mostly metal, is cast into shape, that is ideal for further processing steps, see Wikipedia contributors (2018a). Components manufactured from these ingots depend critically on the composition of the alloy. For this reason, the correct adjustment of the alloy composition and effects changing this composition caused by subsequent manufacturing steps have to be well understood. For safety-critical parts, e.g. turbine blades, the most important factors are the predictability and reliability. This is why the quality of such components can only be achieved with the production of homogeneous and defect-free material, see Appel et al. (2011), Güther et al. (2010).

To achieve the necessary homogeneity the most important factor is to reduce the macro-segregation of alloying elements, both central axis to surface and one end to another, to a minimum. For γ-TiAl-alloys the variation of elements within an ingot, in particular aluminium, can lead to different microstructures than expected and thus lead to different mechanical behaviour. Appel et al. (2016) states that a variation of less than ± 0.3 at% is acceptable for most γ-TiAl-alloys, although some alloy compositions could react even less sensitive to such changes. The highest reliability in components is achieved with ingots, that are as close as possible to the nominal alloy composition for the given material.

The first step of the production of an ingot is the manufacturing of a consumable electrode via hydraulic pressing. The material for the compaction in the press consists of titanium (Ti) sponge, Al and masteralloys. Raw materials for these masteralloys are oxides with Al such as AlNbCr or AlNbMo and are produced via Alumino-Thermic Reduction (ATR). To guarantee the dissolution of high refractory metals the masteralloy is crushed and ground to powder with a particle size of 800 μm. For the final composition the powder is blended and refined by Vacuum Induction Melting (VIM). The resulting material gets crushed again to form granules, which have an advantage over powder for the subsequent manufacturing steps. The γ-TiAl-alloys react

sensitively against impurities or contaminations coming from oxygen (O), nitrogen (N), iron (Fe), copper (Cu) and others. To bring the material in the necessary form of an electrode, the ingredients are placed in the lower die of a hydraulic press and compacted. The electrode is assembled of multiple of these compacted parts, which are welded under an inert argon (Ar)-gas atmosphere, see Güther et al. (2018).

Several melting techniques are used in the production of TiAl-ingots on an industrial scale (cf. Figure 2.5). The mainly used procedures are Vacuum Arc Melting/Remelting (VAR), Plasma Arc Melting (PAM) and Induction Skull Melting (ISM). The benefits and disadvantages of these procedures are discussed in subsections 2.4.2, 2.4.3 and 2.4.4. A technique that is not used for melting of γ-TiAl-alloys is the electron beam melting, because the vaporization of aluminium during the melting process is unstable and thus this process is not reliable enough for the manufacturing of safety-critical components. The final step in the manufacturing of ingots, irrespective of the melting procedure, is the Hot Isostatic Pressing (HIP). It is mainly used to reduce the porosity in the material. For γ-TiAl-alloys the temperatures are $1000\,°C$ to $1200\,°C$, the pressure is in a range of $100\,MPa$ to $200\,MPa$ and the time of HIPing is around $4\,h$, see Appel et al. (2011), Güther et al. (1999, 2018).
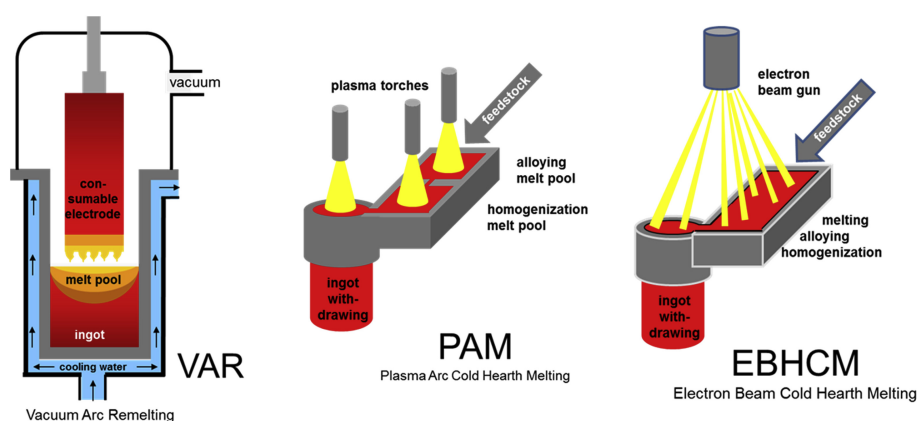

Figure 2.5: Basic production technologies for Ti- and TiAl-alloys. Figure and caption taken from taken from Güther et al. (2018), fig 2, with permission from Elsevier.

2.4.2 Vacuum Arc Melting

In this process called VAR a consumable electrode is melted with a direct electric current (DC)-arc in a metallurgical vacuum environment (0.1-10 MPa). This arc is formed between a water cooled ingot mould made of copper and the electrode. The power supply is attached to the mould (anode) and to the cool end of the electrode (cathode). At the beginning of the process the bottom of the mould is laid out with the material of the electrode to be remelted and to start the initial arc. As the

electrode melts an ingot forms in the crucible. The mould is surrounded by electric coils for electromagnetic stirring of the liquid material. To prevent the arc from striking the walls of the mould, the electrode's size is small compared to the mould. It is possible to melt more than one electrode to form one ingot. This manufacturing step decreases the homogeneity of the ingot, especially at the transition from the first to the second used electrode. After the electrode is fully melted and the process comes to an end, the ingot is referred to as 1 x VAR or primary ingot. To increase the homogeneity further and specify the microstructure, conventional Ti-alloys pass the melting/remelting process two or three times, depending on the specifications of the microstructure. These ingots are then referred to as 2 x VAR and 3 x VAR. Ingots made of γ-TiAl-alloys are manufactured in a 3 x VAR process. Although the composition of the material does not change between 2 x VAR and 3 x VAR, the homogeneity increases significantly for TiAl-alloys of the first generation. β-solidifying γ-TiAl-alloys, e.g. TNM, don't exhibit the necessary homogeneity that is accepted for the final ingot. For this reason this alloy generation requires an additional homogenization step using a VAR skull melting process, see Güther et al. (2018). From one melting/remelting step to another the ingot gets inverted. Also the diameter of the electrode and the mould increase from step to step to prevent the arc from striking the walls and in order to make the electrodes fit the moulds in the subsequent steps, see Appel et al. (2011), Güther et al. (1999), Revil-Baudard et al. (2014).

Figure 2.6 presents a sketch of this process.

The monitored parameters during the VAR process are listed below, see Appel et al. (2011), Güther et al. (2018):

- arc current

- arc voltage

- vacuum level

- melting rate

- electric current in the stirring coils

- depth of the melt pool

The control of these parameters leads to a homogenous microstructure and the required composition of the alloy. The vacuum is necessary to minimize contaminations caused by the surrounding gas or possible water leaks. The arc current and voltage control the melting rate and the temperature at the electrode and the melt pool. For the final 25-30 % of the electrode's length the power is reduced gradually, which prevents defects caused by α-stabilized regions. This procedure also has a positive
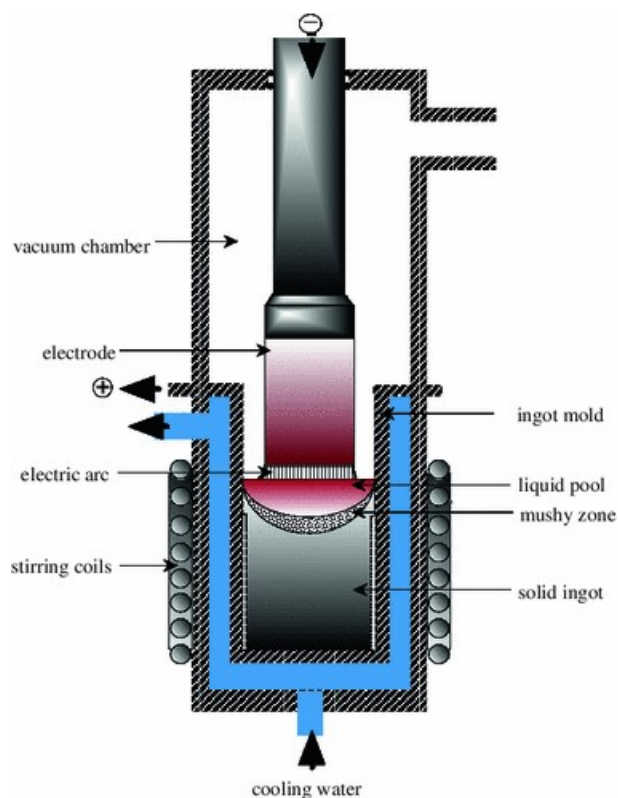
Figure 2.6: Schematic representation of the VAR-process. Figure and caption taken from Revil-Baudard et al. (2014), fig 1, with permission from Springer Nature.

impact on pipe shrinkage and defects caused by it. The electromagnetic stirring is used to increase homogeneity of the ingot, but according to Appel et al. (2011) the evidence whether this procedure is beneficial to the process, is still missing.

Problems that arise during the VAR-process are listed below, see Achtermann et al. (2014), Appel et al. (2011), Güther et al. (2018):

- different melting points of alloy components

- unalloyed Ti granules that drop into the melt

- formation of Ti-rich inclusions

- flaking off unmelted parts of the electrode

- rupture of the finished ingot due to cooling

The dropping of Ti granules into the melt is depicted in Figure 2.7. This unmelted Ti piece forms a so called Ti-rich inclusion. The breakout of these granules is a result of the different melting points of the materials in the first compacted ingot. The melting points of Ti and masteralloys are close to each other and are the highest in the compacted electrode. Al has a significantly lower melting point. Hence Ti granules surrounded by Al break out and fall into the melt. The melting point of

TiAl lies between Ti and Al. As a consequence of these melting points the inclusions could remain in the TiAl matrix even after remelting of the ingots. This phenomenon cannot be fully avoided but suppressed. The right adjustment of the melting rate allows the formation of intermetallic TiAl-phases directly at the face of the melting electrode and thus prevents the formation and the breakout of Ti inclusions. This also describes the greatest weakness of this process used for TiAl-alloys, see Güther et al. (2018).
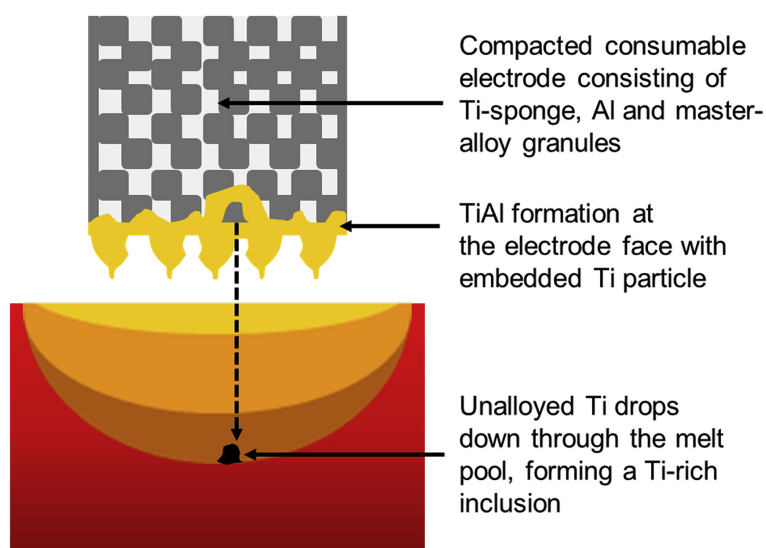

Compacted consumable electrode consisting of Ti-sponge, Al and master-alloy granules

TiAl formation at the electrode face with embedded Ti particle

Unalloyed Ti drops down through the melt pool, forming a Ti-rich inclusion

Figure 2.7: Mechanism of the formation of Ti-rich inclusions in al TiAl ingot during VAR. Figure and caption taken from Güther et al. (2018), fig 3, with permission from Elsevier.

2.4.3 Plasma Arc Melting

The second process depicted in Figure 2.5 is plasma arc cold hearth melting or PAM. It was developed as an alternative to the VAR process. The furnace for PAM can be divided in three parts: (i) alloying melt pool or melting tundish, (ii) homogenization melt pool or refining hearth and (iii) the ingot withdrawing. A plasma torch is used to melt a feedstock. The melt is held in a horizontal water cooled hearth made of copper. After it passes the melting tundish and the refining hearth it is withdrawn vertically to form an ingot, see Blackburn and Malley (1993), Güther et al. (2018), Appel et al. (2011).

The furnace is fed by a feedstock, that consists of compacts, comparable to those described in subsection 2.4.2. The PAM-process also allows the use of premelted ingot material. The total unit operates under inert conditions. This is accomplished by two steps: (i) evacuation of the system with vacuum pumps and (ii) filling the

system with an inert gas under a pressure of 1.1 bar. Helium (He) is preferred over Ar due to its higher conductivity and higher ionization potential, which leads to a higher thermal input in the material. In the course of operation there is a steady input of plasma torch gas. To maintain a constant pressure in the system a pressure relief valve is installed. To monitor the atmosphere in the system the leak rate is measured or a mass spectrometer is installed, which is the preferred method, see Blackburn and Malley (1993), Appel et al. (2011).

Before the process starts with the first struck plasma arc, the hearth is laid out with compacted so called "hockey pucks". Only after these are melted more material is added by the feedstock. TiAl-alloys are reactive with its surrounding at elevated temperatures. For this reason a so called "skull", a layer of solid alloy, is formed at the bottom of the water cooled hearth. The plasma torches are programmed to move over the material to enable homogeneous melting. Other contributors to the homogeneity are gravity and time. As the material flows in the hearth reactive contaminants are able to dissolve and high density contaminants sink and become trapped at the bottom in the semi-solid material. To increase the homogeneity of γ-TiAl-alloys an arrangement of three hearths is employed before the material is withdrawn. The dwell time of the liquid alloy in the hearth is independent of the process time and ingot size. For this reason it is possible to control the reactions taking place in the melt. Another advantage of the multiple crucible arrangement is the flat and horizontal hearth, that enables the dissolution of defects caused by O and N, without the presence of a deep melting pool. The depth of the melting pool increases segregation. The ingot withdrawing unit is placed at the end of the melting and refining crucibles. This part of the system consists of a fixed crucible with a movable bottom, both made of copper and water-cooled. Once the material enters, the bottom is lowered continuously, forming the ingot. A plasma torch is placed over the withdrawing unit to keep a liquid metal pool at the top of the ingot, that is stirred with electromagnetic coils, see Blackburn and Malley (1993), Appel et al. (2011).

The surface of such ingots is rougher compared to VAR manufactured ingots. The quality of the surface can be increased by reducing a parameter called "dither". It describes the amplitude of an oscillating motion of the ram that is superimposed on the withdrawing motion. A low amplitude of the dither improves the surface quality. Another factor influencing the surface quality is the ingot power density, which is dependent on the torch gas and the length of the arc, see Blackburn and Malley (1993), Appel et al. (2011).

Problems that arise during the PAM-process are listed below, see Appel et al. (2011), Güther et al. (2018):

- unmelted regions of compacts remain in the hearth and influence composition of the ingot

- pores that arise during the withdrawing process cannot be removed by subsequent manufacturing steps like forging or extrusion

- fast withdrawing rates lead to an inhomogeneity of the ingot

- fast withdrawing rates lead to an unsymmetrical solidification at the top of the ingot

The optimization of the PAM process starts with the optimization of the compacted feedstock material. Fine granules and powders show a higher homogeneity in the ingots. A further gain of homogeneity can be achieved by double or triple melting/remelting of the material. Also an increased dwell time of the material in the melting and refining hearth and the size and depth of the melt pool increase homogeneity, see Appel et al. (2011).

Table 2.1 compares the VAR and PAM processing of γ-TiAl-alloys, see Güther et al. (2018), Appel et al. (2011).

Category	PAM	VAR
Direct processing costs	Moderate	High due to inert gas consumption
Homogeneity	Low for 1 x VAR, good for 2 x VAR and 3 x VAR	Good for 1 x PAM, high for 2 x PAM
Materials soundness	Reasonable, depends on solidification mechanism and, thus, on ingot diameter	Reasonable, depends on solidification mechanism and, thus, on ingot diameter
Surface quality	Smooth, as cast surface	Craggy, depends strongly on process parameters
Ingot geometry	Cylindrical	Multiple geometries possible
Recycling	No recycling capability	Unlimited recycling capability
Inclusions	Possible, due to diverging melting points of alloy components	Little, due to possibility of "trapping" the inclusions
Defects	Pipe shrinkage and formation of α-stabilizing regions	Can be omitted, due to shallow melt pool depth

Table 2.1: Differences regarding process parameters of PAM and VAR.

2.4.4 Induction Skull Melting

ISM is a melting technology, that uses a cylindrical water-cooled copper crucible to melt a material. The heat is generated by induction coils, that surround the crucible and run with medium frequency. As the name suggests, it is a skull melting technique and therefore does not allow for contact of the melted material with the walls of the crucible. As a consequence the pickup of impurities from the crucible is minimized. The melting takes place under vacuum or an inert atmosphere with Ar. The liquid material is mixed by the induction process and poured by tilting the crucible into ingot moulds or component moulds (cf. Figure 2.8).
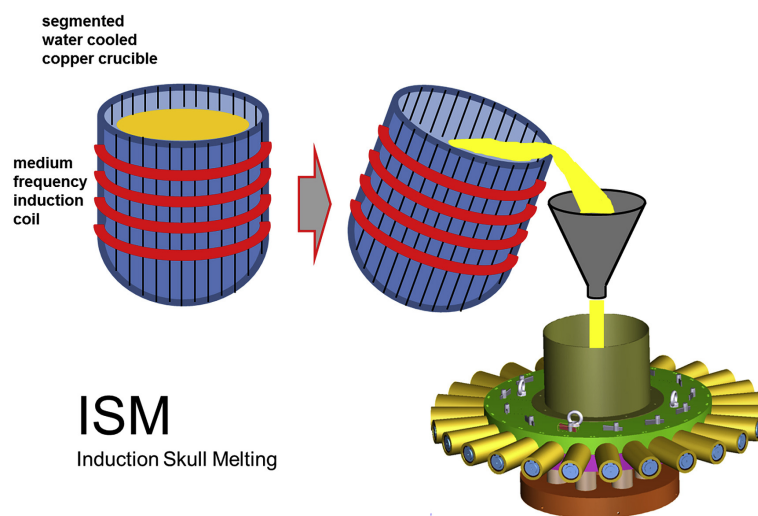

Figure 2.8: Sketch of ISM technology. ISM offers a one-step revert conversion into semi-finished products. Figure and caption taken from Güther et al. (2018), fig 14, with permission from Elsevier.

The process can be used as a preceding step to casting or for recycling of unused material like funnels, feeders or casting plates. It is a clean, cheap and flexible technique with regard to alloy composition and the use of primary material. The use of vacuum has the disadvantage, that volatile components, e.g. Al, evaporate and change the composition of the alloy. The relatively small superheat in this process does not allow for a long holding time before the liquid material is poured for subsequent manufacturing. For this reason the dump pour technique is used, which leads to a chaotic flow inside the mould. This increases the risk of defects, like entrapped bubbles, trapping of oxide films or surface break-up. Oxide films effect the solidification by acting as heterogeneous nucleation sites, which leads to increased porosity, see Güther et al. (2018), Appel et al. (2011).

2.4.5 Centrifugal Casting

Several casting methods are developed for γ-TiAl-alloys and can be processed using conventional casting equipment. It is the most cost effective method in the manufacturing of near net shape components made of TiAl. The success of the production with this method depends strongly on the processed alloy composition. For γ-TiAl-alloys the process of centrifugal casting as an intermediate step in ingot manufacturing has been established.

The two types of centrifugal casting used for γ-TiAl-alloys are horizontal and vertical centrifugal casting. The horizontal centrifugal casting is used for components with an axis of revolution such as ingots. The vertical centrifugal casting is used for non-axisymmetrical components. The main principle of this method is that molten metal is poured into one or multiple rotating moulds. The centrifugal forces force the material to fill the moulds and keep the melt under pressure until it solidifies completely, see Appel et al. (2011). The horizontal centrifugal casting of cylindrical ingots is depicted in Figure 2.9 and 2.8 each with a different method of manufacturing the melt.
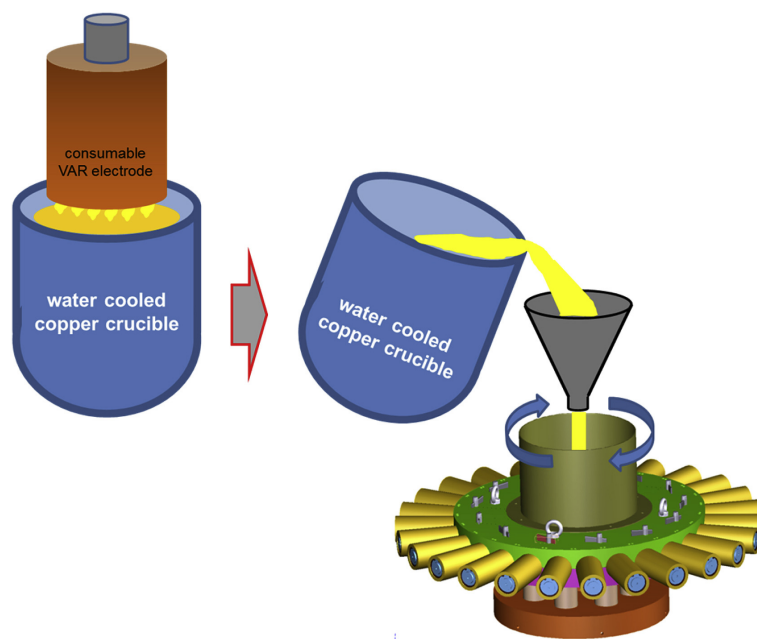

Figure 2.9: Sketch of VAR Skull Melting and subsequent centrifugal casting in permanent steel moulds. Figure and caption taken from Güther et al. (2018), fig 8, with permission from Elsevier.

For the particular application of ingots that are used as electrodes in atomization processes the VAR melted and double VAR melted material does not reach the necessary homogeneity. For this reason, the route of VAR skull melting with subsequent centrifugal casting is applied. A previously VAR remelted ingot is melted and kept liquid in a crucible. For the entire process the melt is in motion through electromagnetic

stirring. This procedure is able to dissolve any high density contaminations such as Ti-rich inclusions. The process has a defined energy consumption, which sets the time used for heating the material. Once the limit is reached the arc is turned off and the ingot is withdrawn from the crucible. By tilting the crucible the melt is poured with a defined speed into the centrifugal casting unit, see Güther et al. (2018).

With this additional step the homogeneity of the ingots is increased further and the material's soundness is the highest for the discussed semi-finished products. At the end of the centrifugal casting the demoulding and cutting off of the feeder takes place. The cut off part does not reach the requirements regarding defects and homogeneity for subsequent manufacturing steps. It is used as recycled material for the ISM-process. The final product of this step is used as forging stock, machining stock and as electrodes for atomization processes, see Güther et al. (2018).

2.4.6 Atomization Processes

The term atomization processes describes multiple processes, that use inert gas to atomize a stream of melted material into metallic powder particles. These manufacturing steps are technologically challenging. In particular for γ-TiAl-alloys the difficulty is the high melting point (1550°C for TNM) and the realization of the process under inert gas atmosphere and with no contact to ceramic crucibles. The reason for this are the high reactivity of the alloy at elevated temperatures, both with the material of the crucible and the surrounding gas atmosphere. All of the techniques exhibit three steps: melting, atomization and solidification. These techniques have also in common the stream of melted metal, that passes through a nozzle. At the nozzle a jet of inert gas, such as Ar or He hits the stream with high velocity and breaks it up into particles. For economic reasons most manufacturers use Ar over He. Appel et al. (2011) distinguishes two types of atomization: (i) free fall or open stream atomization and (ii) closed loop or confined-feed atomization. Method (i) is depicted by a stream that freely falls through a nozzle before the atomization occurs. (ii) The melt is transferred to a high pressure atomizing gas. The processes discussed in this thesis are all of type (i) and differ solely by its melting technique. A general setup of an atomization unit is depicted in Figure 2.10, where the units mounted at the top differ in the melting technique. The bottom part is the cooling tower, where the atomized particles solidify, cool down and accumulate at the bottom. From there the powder is separated due to the particle size and collected for further processing steps, see Appel et al. (2011), Clemens et al. (2018), Sun et al. (2017).
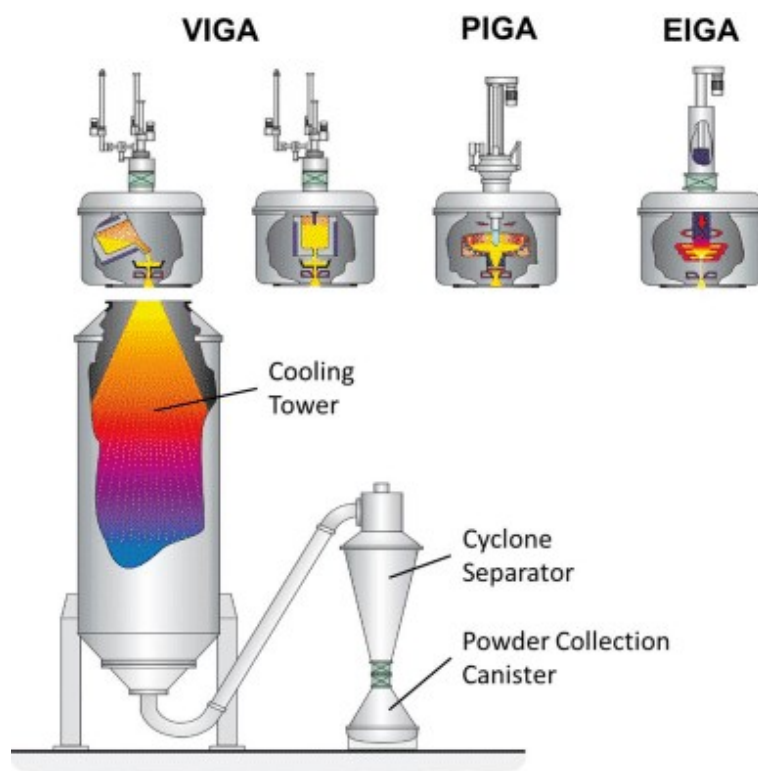
Figure 2.10: Manufacturing processes for TiAl-alloy powders. Figure and caption taken from Clemens et al. (2018), fig 2, with permission from Springer-Verlag Wien.

Not only the melt stands out with its high reactivity but also the powder. The hot solid particles are susceptible to O, N and carbon (C) impurities. Also at ambient temperature the powder shows a high reactivity to O. For this reason, the powder must not be exposed to air to counteract the enrichment of O, see Gerling et al. (2004), Clemens et al. (2018).

With increasing velocity of the atomization gas the particle size decreases. At the nozzle the melt drop changes its direction of motion and cools down rapidly. Cooling rates of 2×10^5 K/s have been reported for particles with a diameter of 45 μm. These cooling rates effect both, the surface tension of the particle and hence the shape, and the microstructure of the material. A homogeneous and fine grained microstructure is created with phase fractions that are not in thermodynamic equilibrium. Gas atomization leads to particles with almost perfect spherical shape. A defect that occurs is the formation of so called satellites, that are a consequence of colliding particles, see Clemens and Mayer (2015), Appel et al. (2011), Gerling et al. (2004).

After atomization the powder is separated into fractions with a certain particle size, to ensure homogenous mechanical behaviour. Particular for TiAl powders the high hardness of the material does not allow for cold compaction as a subsequent manufacturing step. For this reason, the powder is filled in near net shape forms and HIPped.

This manufacturing step reduces porosity. Inert gas from the atomization that might be trapped in the material gets compressed to such an extent that no porosity due to this gas inclusion is detectable. In a subsequent manufacturing step, e.g. forging, these pores could open and lead to defects called thermally induced porosity (TIP), see Appel et al. (2011), Clemens et al. (2018).

Factors that influence the powder quality are summarized and listed below, see Appel et al. (2011):

- melting technique

- particle size and particle size distribution

- particle shape

- flowability of the powder

- gas pressure in the nozzle

- melt stream diameter

- melt temperature and melt superheat

- cooling rate

- nozzle arrangement

Two melting techniques for the atomization process are described in the following subsections.

2.4.6.1 Plasma Melting Inert Gas Atomization

Plasma melting Inert Gas Atomization (PIGA) is a process that uses a plasma torch to melt prealloyed material for atomization. The total unit is under an inert gas atmosphere, both to ensure the quality of the melted material and produced powder and to enable the use of a plasma torch. It is considered a cold crucible technique with no ceramics. A detail of this melting process is depicted in Figure 2.11, see Appel et al. (2011), Gerling et al. (2004).

The system has to be evacuated and flooded with Ar or He repeatedly to ensure a completely inert atmosphere. Additionally selected parts are heated to eliminate moisture. To start the melting process, the prealloyed material is placed in the water-cooled copper crucible. The plasma torch melts the material until the necessary temperature is reached. At the bottom of this crucible there is a channel that leads to the atomization nozzle. This channel is heated additionally with induction coils
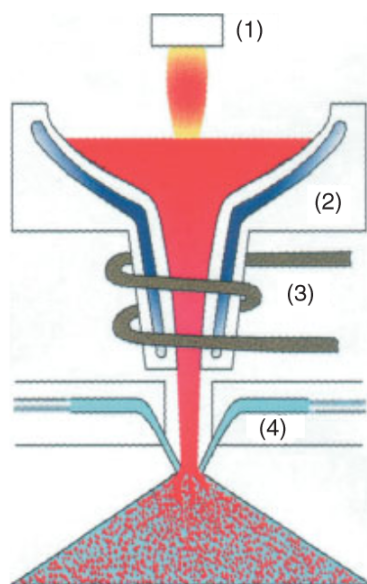
Figure 2.11: Schematic drawing of the Plasma Melting Induction Guiding Gas Atomization PIGA technique. (1) Plasma torch, (2) Cold Copper Crucible, (3) Induction Heated Cold Copper Funnel, (4) Gas Nozzle. Figure and caption taken from Gerling et al. (2004), fig 3, with permission from Wiley-VCH.

to ensure the required superheat and avoid cooling of the molten material. The connection between the crucible and the atomization nozzle opens once the atomization process starts. The geometry of the funnel and the electromagnetic forces constrict the melt to a thin stream. This allows the production of smaller particles with a narrower particle size distribution. The system is designed to produce comparatively large amounts of TiAl powder (Gerling et al. (2004) describes a melt flow rate of 250 kg/h) and has the advantage of high homogeneity of the melt. The disadvantages of this melting technique are high costs due to inert gas usage, complex safety precautions due to the use of plasma torches and the amount of electric power that is needed to operate the plasma torches and induction coils, see Appel et al. (2011), Gerling et al. (2004).

2.4.6.2 Electrode Induction Melting Gas Atomisation

The EIGA process uses a consumable electrode, that is melted with induction coils for further atomization. A schematic representation of this melting process is depicted in Figure 2.12. The electrode is mounted to a rotating part at the top end. This allows to rotate the electrode around its central axis and lower it toward the induction coils. The rotation ensures a symmetrical melting of the tip of the electrode. The induction coils are located at the bottom end of the melting chamber. These are arranged in
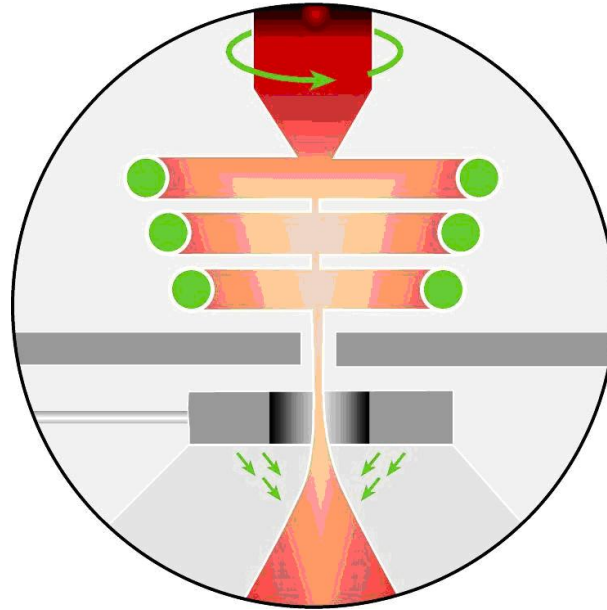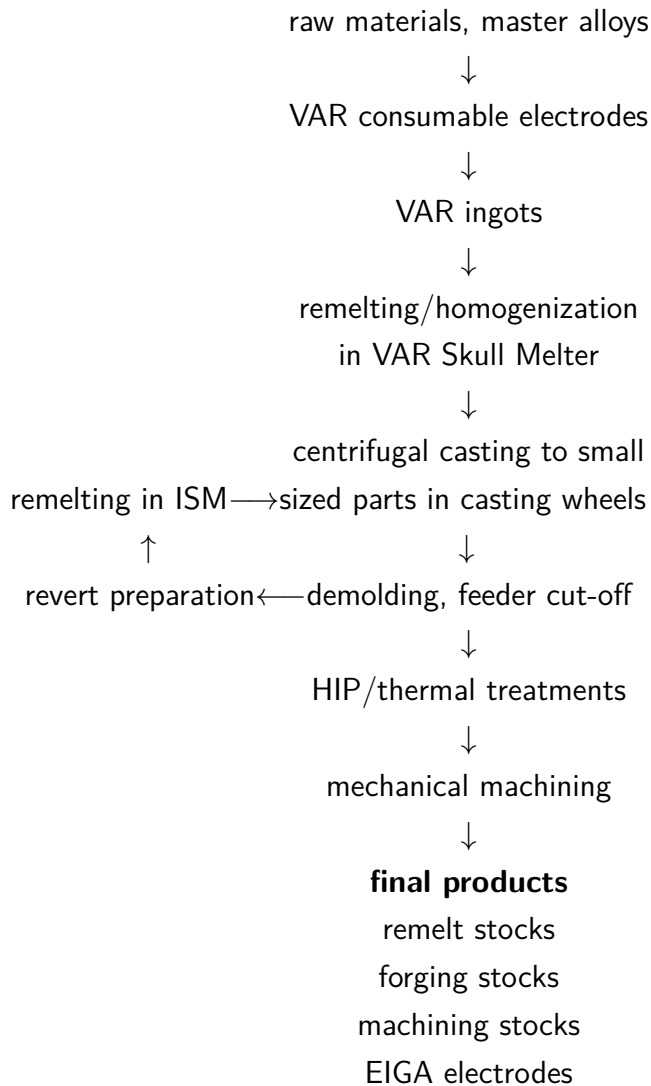
Figure 2.12: Melting of an electrode with the Electrode Induction melting Gas Atomization (EIGA) process. Figure taken from LPWtechnologies (2018)

a cone-shape with an opening angle that depends on the material and the melting speed. The rotation speed is at around 5 rpm. The induction coils, that operate at medium to high frequencies, heat the tip of the electrode until it reaches its melting point. The melt accumulates at the tip and is superheated up to 100 °C above the melting point. At this point the melt drops into the atomization nozzle forming a thin melt stream. The electrode is lowered towards the induction coils with the same speed as the material melts away. The control system monitors among other things the distance between the electrode and the induction coils and keeps this distance at a constant value for the total process time, see Hohman and Ludwig (1994), Appel et al. (2011).

The EIGA process allows completely contact free melting of γ-TiAl-alloys. Thus the material is only in contact with the inert gas and contaminations are prevented from entering the material. Contaminations or irregularities, that can still be found in the final product can be traced back to inhomogeneities and defects in the electrode from preceding manufacturing steps. For this process Gerling et al. (2004) states a production rate of $50\ kg/h$, which is considerably less compared to PIGA. An advantage of the the EIGA process is the slightly smaller mean particle size of 55 μm compared to PIGA with 77 μm.

Güther et al. (2018) describes a production chain for γ-TiAl-alloys for semi-finished products, that is already in use. The flowchart of this production chain is depicted below.

raw materials, master alloys

↓

VAR consumable electrodes

↓

VAR ingots

↓

remelting/homogenization
in VAR Skull Melter

↓

centrifugal casting to small

remelting in ISM⟶sized parts in casting wheels

↑   ↓

revert preparation⟵demolding, feeder cut-off

↓

HIP/thermal treatments

↓

mechanical machining

↓

final products
remelt stocks
forging stocks
machining stocks
EIGA electrodes

This flowchart describes the multiple steps that have to be taken to manufacture semi-finished products of γ-TiAl-alloys. The possibility to produce near-net-shaped components from prealloyed powders is probably the greatest advantage of this production route. For this reason, the following chapter describes one critical step of this route from an engineering point of view. The production rate of the EIGA process depends on multiple factors. One key factor is the size (diameter) of the electrode used for atomization. Measurements during the process are challenging, especially regarding accuracy. To gain more information on the processes that take place during the melting of the electrode, a numerical model was set up which will be described in detail in the following chapter.

3 Modelling

For building the numerical model the commercial FEM software ABAQUS version 6.14 was used under the operating system Ubuntu 18.04. The problem is axial-symmetric which allows for a two dimensional (2D) model of the meridian section of the electrode.

For calculating the residual stresses induced by heat during the process two models are required. Firstly it is necessary to calculate the temperatures at every point and at every time step. With this information it is possible to start the stress analysis and use the temperature field calculated in the heat conduction analysis as thermal load.

3.1 Geometry Modelling

The component for the simulation is a cylindrical rod with a 45° tip at one end (cf.: Figure 3.1). The length of this part is 1 m and the used diameters are 40 mm and 80 mm. This geometry was chosen, because it represents standard rods for electrodes for melting processes. As stated by Ebel et al. (2011) it is possible to use rods with diameters up to 140 mm.
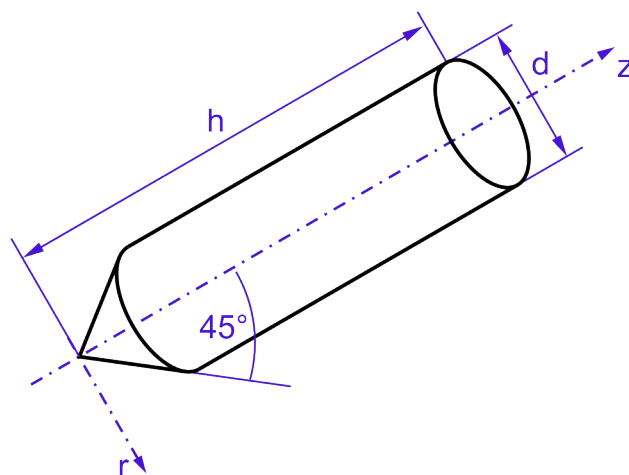

Figure 3.1: Basic geometry of the electrode

Since the geometry is axially symmetric it is possible to represent the electrode for the simulation with a 2D-model. The axis of revolution of the cylinder also represents the symmetry axis in the 2D-model. Therefore it is sufficient to display only one side of the electrode. In the software ABAQUS the axial symmetry is defined by means of the use of a particular type of elements. These elements require not only a definition of a symmetry axis but it is also necessary to apply radial boundary conditions on nodes located at this axis, see Abaqus-Documentation (2018).

ABAQUS provides a graphical user interface (GUI) that is a part of Complete Abaqus Environment (CAE) to create geometries for the simulation. For more complex components it is useful to design the geometry in a separate computer-aided design (CAD) package, and import it into ABAQUS. Regardless of how the geometry is created, for further calculations ABAQUS has to generate an input (inp.)-file with all the information of the part. Depending on the mesh size and the choice of element type, the component is discretized by a sufficiently large number of elements. The inp.-file contains all the information of the geometry, i.e. nodal coordinates with all element connectivities. It is possible to create the inp.-file directly without using the GUI of the software.

For this particular geometry of the rod shown in Figure 3.1, the part for the simulation is generated manually by editing a text-file, that can be added to the inp.-file of ABAQUS. To create a single node for an axially symmetric model, a node number has to be defined and the coordinates r and z have to be assigned to it. The r-direction corresponds to the global 1-direction and the z-direction corresponds to the global 2-direction. The first coordinate, i.e. r, has to be greater than or equal to zero, since negative coordinates are nor allowed in an axially symmetrical model. The symmetry axis is defined as z-axis. The degrees of freedom one and two are u_r and u_z respectively, see Abaqus-Documentation (2018).

The node numbers and the corresponding coordinates have been generated by a MATLAB script. It allows to number consecutively the nodes in a controlled order. For this reason it is possible to associate the position of a node with its number. Figure 3.2 presents the pattern how the nodes are numbered. For the corresponding MATLAB script the reader is referred to Appendix A1.

The first node is located at the tip of the electrode and has the number 11101. The last two digits indicate the position on a particular edge and the first three digits indicate the position of the edge starting from the bottom. With this pattern it is possible to fill one edge with up to 99 nodes and have up to 888 rows. Leading zeros are avoided in this arrangement of numbering to assure consistency with all text based software tools. The total number of nodes depends on the size of the mesh and the
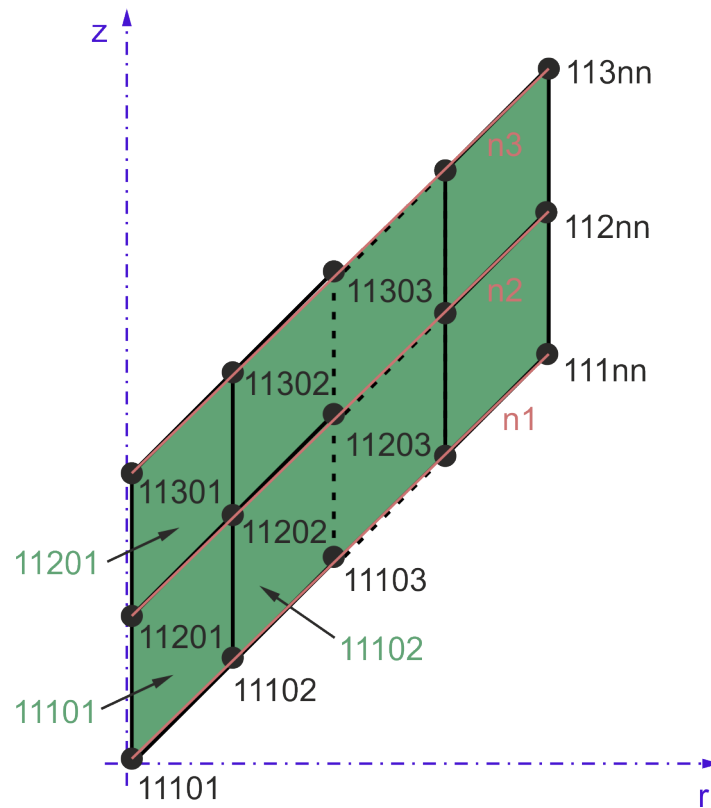
Figure 3.2: Pattern of node and element numbering

geometry. Since the length of the rod is limited to 1000 mm the smallest possible element or mesh size is 1.12 mm.

The coordinates for the nodes are calculated depending on the angle of the tip of the rod and the element size. Once every node is located in the geometry, elements are generated with a similar pattern, connecting the four surrounding nodes to one element, as shown in 3.2. For details of the code the reader is referred to Appendix A1.

The used routine for numbering limits the choice of elements to linear elements with four nodes. The precision of the results can be influenced by the size of the mesh.

3.2 Heat Transfer Modelling

The heat transfer in the simulation is modelled by applying boundary conditions, external heat sources and interactions with the surrounding medium. Figure 3.3 illustrates schematically how the heat transfer is defined in the model.
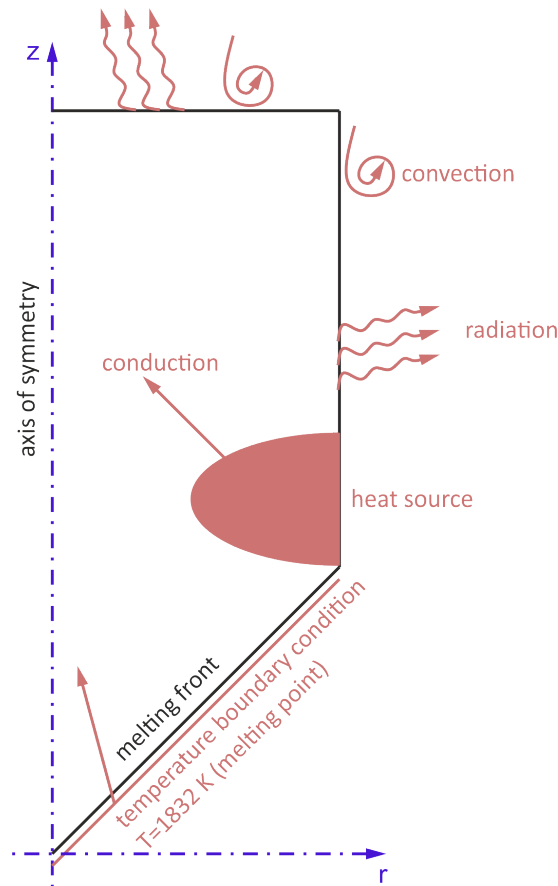
Figure 3.3: Model of heat transfer of an EIGA electrode

3.2.1 Modelling of Conduction

Heat transfer by conduction is governed by the thermal conductivity λ as described in equation 2.1. Figure 3.4 contains the values of λ dependent on temperature T. As evident from this diagram the values are in the range of 10-20 W/mK. For comparison the thermal conductivity of steel ranges between 15 W/mK for high alloy and 55 W/mK for low alloy steels. The values for copper are around 400 W/mK, see VDI (2013).

3.2.2 Modelling of Temperature Boundary Conditions

The bottom edge of the electrode, the one that reaches the melting temperature T_m, is modelled by applying a temperature boundary condition. This is a Dirichlet boundary condition with the values of the temperature at the nodes of the melting edge. T_m is prescribed as 1559 °C (1832.15 K). This boundary condition induces a heat flux into the electrode and is representative of the heat sources that lead to the melting of this edge.
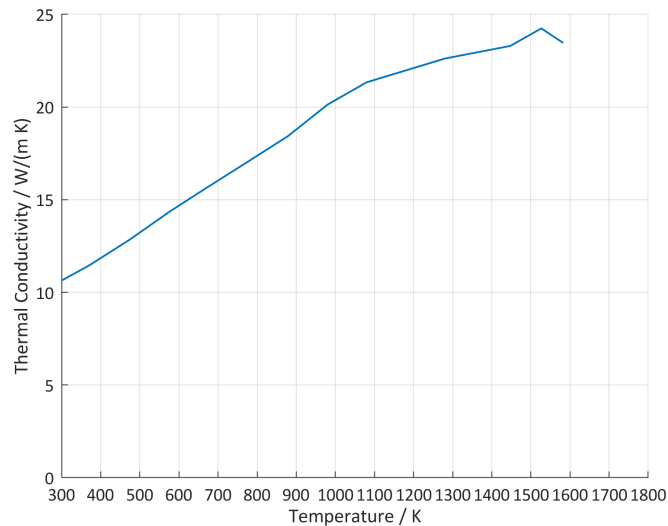
Figure 3.4: Temperature dependent thermal conductivity. Data received from Institut für Metallkunde und Metallische Werkstoffe (IWM), Montanuniverstität Leoben.

Since the material melts away at this part of the model, it is necessary to move this boundary condition with the speed of melting through the electrode. It is assumed that the average velocity of this process is 50 mm/min, which leads to a production volume of 60 kg/h of metal powder with a diameter of 80 mm of the electrode. This is according to Appel et al. (2011) an average value of powder production. To apply a boundary condition, specific nodes have to be selected and the prescribed temperature assigned to these nodes. A more common approach is to define node-sets that contain all the nodes located at a given geometry and apply the boundary condition on a whole node-set. To model the movement of the melting edge, node-sets for every row of the mesh have been generated. The MATLAB-routine for creating the geometry already provides a consecutive numbering of the nodes in the mesh. For details on the code the reader is referred to Appendix A1. An extension of this routine assigns the nodes of each row to a separate node-set, as Figure 3.2 shows. For every node-set, a separate step of the simulation is generated. Additionally a step-time is calculated dependent on the melting velocity and the element size. Thus each step takes exactly the time that is needed to melt one row of elements of the mesh. The boundary condition jumps to the next node-set in the next step.

3.2.3 Modelling of Interactions at Boundaries

There are two interactions at boundaries. One is the thermal radiation of the part with its surrounding and the other one is the convection at the surface.

To model the radiation, the surfaces that are in contact with the surrounding medium have to be defined. As described in equation 2.16 the heat flux released by thermal radiation solely depends on natural constants, the emissivity and the temperature difference between the part and its surrounding. Due to the forth power of temperature this heat flux contributes to the cooling of the electrode at high temperatures only. For every simulation calculated within this thesis the ambient temperature T_∞ has been set to 25 °C (298.15 K). The emissivity has to be presumed based on plausible analogies, because measured data were not available at the time of this thesis. Based on the literature review the value can change up to a factor of 100 for the same material dependent on its surface condition, e.g. polished or oxidized, see Stephan (2008). For every simulation in this thesis the value for the emissivity is set to a constant value of 0.1 over the total temperature range. This is based on the assumption that the surface is inhomogeneous after centrifugal casting.

The second interaction is the convection at the surface of the part. The heat flux depends on equation 2.2 and needs the information on the heat transfer coefficient α_k. In ABAQUS this coefficient can be defined as a function of temperature, see Abaqus-Documentation (2018). As described in section 2.2.2 α_k depends on multiple factors. In this simulation the influence of temperature, orientation of the flow and the geometry of the surface are considered. These calculations are executed separately and only the temperature dependent film coefficients, that contain all the other information, are implemented in the FEM-model. Four different α_k's are calculated. The first two describe the behaviour during cooling for the two surfaces of a horizontally positioned cylinder. The other two represent the surfaces of a vertically positioned cylinder:

- flat and vertical surface
- curved and horizontal surface
- flat and horizontal surface
- curved and vertical surface

The results for these four α_k's are presented in table 3.1. This interaction makes up the heat flux at low temperatures. For further information on the calculation the reader is referred to Appendix A3.

In every step of the simulation the interactions have to be defined for every surface with its corresponding sink temperatures and values for the coefficients. Thus it is possible to use one set of coefficients for the cooling of a horizontally positioned part and another set for a vertically positioned part.

Temperature	Heat transfer coefficients in mW/mm^2K			
K	vertical cylinder vertical surface	vertical cylinder horizontal surface	horizontal cylinder horizontal surface	horizontal cylinder vertical surface
273,15	0,004361124	0,062138024	0,052793932	0,032627264
298,15	0,00016057	0	0,000223288	0,000118106
348,15	0,005112046	0,071497593	0,061992013	0,038321303
448,15	0,006579012	0,08789642	0,080088476	0,049538907
548,15	0,007157569	0,096201723	0,08709071	0,053864844
648,15	0,007446386	0,101795496	0,090480022	0,055947567
748,15	0,007604231	0,10602341	0,092240339	0,057020121
848,15	0,007690614	0,109416784	0,093113501	0,0575432
948,15	0,007738808	0,112272829	0,093515423	0,057775037
1048,15	0,007760747	0,114712904	0,093594581	0,057807637
1148,15	0,007767295	0,116861568	0,093485452	0,057724314
1248,15	0,007763183	0,118771741	0,093247127	0,05756159
1348,15	0,007749441	0,120459763	0,092892517	0,057327402
1448,15	0,007731997	0,122006795	0,092494355	0,057066711
1548,15	0,007706914	0,123375355	0,092004101	0,056748081
1648,15	0,007687515	0,124711147	0,091586925	0,056477813
1748,15	0,007663669	0,125926097	0,091116216	0,05617338
1848,15	0,007635225	0,127010012	0,090590739	0,055835309

Table 3.1: Temperature dependent heat transfer coefficients

3.2.4 Modelling of Additional Heat Sources

Figure 3.3 presents two ways of heat input in the model. The second one is the heat input due to a prescribed heat flux. This heat flux represents additional induction coils, that are not already represented by the temperature boundary condition. In the actual process the electrode melts on one end and the liquefied material drops into the gas atomization nozzle due to gravity. The electrode is fixed at the other end and moves downwards to the induction coils. The distance to these induction coils stays the same for the entire process, as the electrode is lowered continuously. In the simulation this movement is done by the heat sources and the electrode is fixed. The User Subroutine (US) DFLUX is applied to carry out the movement of the heat sources.

DFLUX allows to define heat fluxes, that are distributed nonuniformly as a function of position, time, temperature, element number, integration point number in a heat transfer analysis. It will be called for every flux integration point for each element-based nonuniform distributed flux definition. It uses nodes as flux integration points for heat transfer elements, see Abaqus-Documentation (2018).

The value of the resulting heat flux q_{df} in the US is modelled by the function in equation 3.1, with a_{df}, b_{df} and c_{df} as coefficients of an exponential function calculated

according to figure 3.5, r and z as the instantaneous coordinates of the calculated integration point, z_{coil} as the current position of the induction coil relative to the global coordinate system, and Q_{amp} as a factor to scale the maximum of this function.

$$q_{df} = \left(a_{df} e^{b_{df} \ r} - c_{df}\right) \cdot \left(e^{-(0.005(z-z_{coil})^2)}\right) \cdot Q_{amp} \qquad (3.1)$$
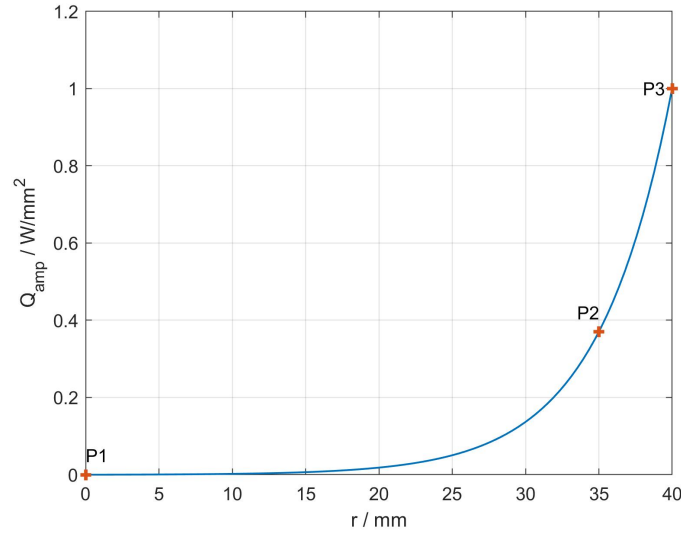

Figure 3.5: Function of the heat flux along r for a cylindrical geometry

Figure 3.5 shows the distribution of the amplitude of the heat flux along the radius of the electrode. The curve is normalized, such that the heat flux on the central axis at point P1 obtains the value 0 and at the surface at point P3 the value 1. P2 is set to 0.37 with a distance of 5 mm to the surface. These coordinates have been chosen such that the influence of the skin effect is captured, which appears in conductors, that are operated with alternating electric current (AC). The density of electric current is largest at the surface of the conductor and decreases with greater depths. According to Wikipedia contributors (2018b) the density of the electric current decreases with an exponential function. The skin depth is the distance from the surface at which the value drops to 0.37 and thus defines the coordinates of P2. The skin depth of 5 mm is assumed to keep the gradient small. The heat generated by an electric current due to induction is proportional to the electrical power and thus to the square of the electric current.

The second part of equation 3.1 describes the decay of the heat flux in z-direction of the electrode. This is an assumption solely made to obtain a smooth curve. Figure 3.6 shows a plot of the function from equation 3.1 with Q_{amp} set to 1. This figure also shows that the heat flux generated by an induction coil has major influence at the surface and very little effect towards the center.
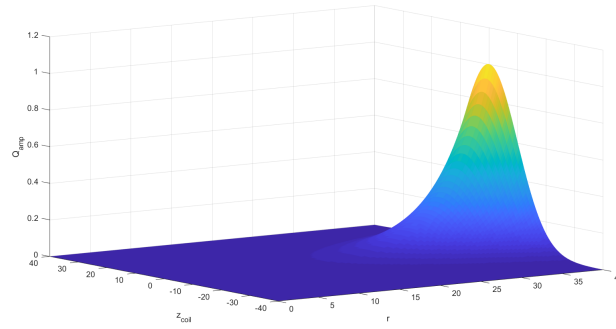
(a) 3D
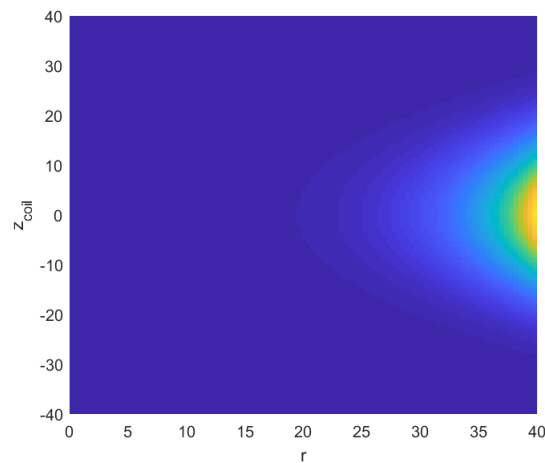
(b) topview

Figure 3.6: Function of the heat flux for DFLUX US

To model more than one heat source the US DFLUX is modified such that the integration points are queried in a sequence of IF and ELSE IF loops. Each loop calculates the value of the heat flux for the given integration points separately. Thus it is possible to change the maximum value of the function for each heat source.

For further details of the code of the US DFLUX the reader is referred to Appendix A2.

3.2.5 Modelling of Latent Heat

Latent heat is energy that is released or absorbed due to a phase transition. It changes the state of substance at a constant value of temperature. The phase transition can be an actual change of the phase, e.g. solid to liquid, but can also occur at phase transitions from one crystallographic structure to another, e.g. α to β, see Lock (1996).

The measurement of latent heat is performed with calorimetry, where the temperature dependent specific heat c_p can be calculated. Figure 3.7 shows the raw data of the c_p-measurement. This data was fitted with a polynomial function to calculate the area between a linear specific heat capacity and the peak caused by latent heat. This area represents the energy that is needed to perform the phase transition α_2 to γ. It is implemented with the solidus temperature of 1273 K and the liquidus temperature of 1573 K.
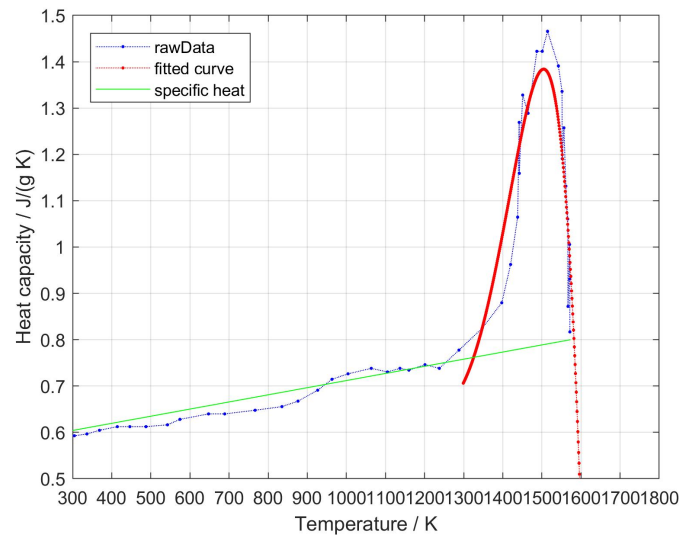

Figure 3.7: Temperature dependent specific heat with effects of latent heat due to phase transition. The red line represents a fitted polynomial of the raw data curve for the calculation of the latent heat.

3.3 Mechanical Stress Analysis

The mechanical stress analysis is performed on the basis of the results from the heat transfer analysis. The temperature difference between the initial temperatures and a predefined temperature field causes thermal strains if the material expands dependent on the temperature. The predefined temperature field can be defined by means of a previously generated results file. In this case ABAQUS reads the results for every time step and integration point into the mechanical analysis and uses the temperature as load for this analysis, see Abaqus-Documentation (2018).

One way to describe thermal expansion is the derivation of the total elongation due to temperature change. The software ABAQUS requires another form for the thermal expansion coefficient α, i.e. the total thermal expansion from a reference temperature (c.f.: Figure 3.8, see Abaqus-Documentation (2018). α_1' and α_2' are the resulting tan-
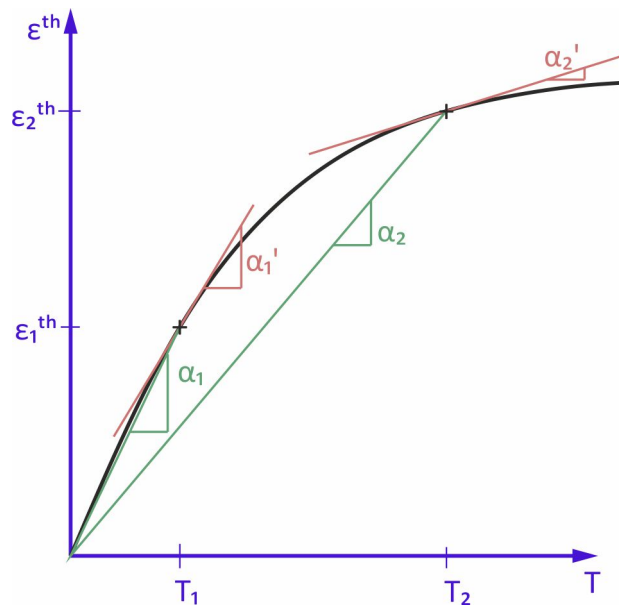
Figure 3.8: Thermal expansion in ABAQUS represented by α_1 and α_2

gents of the temperature dependent curve of elongation. By building the secant from the point of origin the thermal expansion coefficient for ABAQUS can be calculated, which is represented by α_1 and α_2 in Figure 3.8.
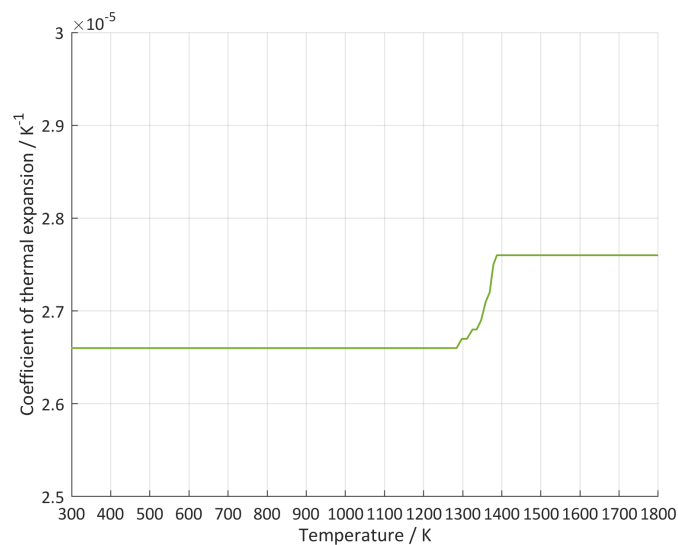

Figure 3.9: Thermal expansion for ABAQUS

For measuring the expansion of the material during heating and cooling, dilatometer-experiments were carried out at IWM. This data is taken and the necessary coefficient of thermal expansion for ABAQUS is calculated. The results are shown in Figure 3.9. Each point of this curve corresponds to a slope of the temperature dependent α in Figure 3.8.

The elastic behaviour of a material is governed by the material parameter Young's[1] modulus. Figure 3.10 shows the temperature dependency of the Young's modulus of TNM. The blue line represents the measurement performed by IWM and the red line an extrapolation. This extrapolation sets the Young's modulus to a very low value at the melting point. This feature makes it possible that the molten parts of the electrode do not influence the stress field of the remaining electrode. To avoid problems in the numerical calculations the value must not drop to 0.
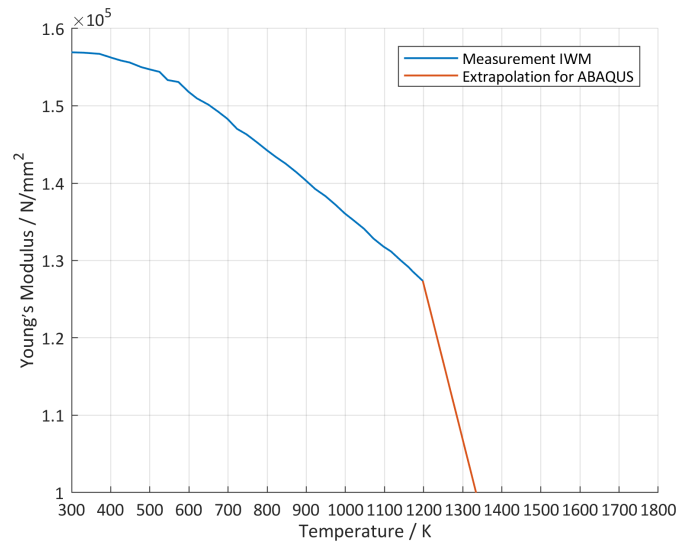

Figure 3.10: Measurement of temperature dependent Young's modulus performed by IWM and extrapolation for higher temperature values for ABAQUS.

Once the stress in a material exceeds a certain value called yield strength, deformations remain in the material due to plasticity, even if it is no longer under load. Therefore, the flow behaviour of the material must be characterized in the relevant temperature interval. The used values for the plastic behaviour of TNM are shown in table 3.2. The data is taken from Schloffer (2013) and Schwaighofer et al. (2014a). The low number of data points is due to missing measurements of these parameters for the total temperature range from ambient temperature to the melting point. In between these data points ABAQUS applies a linear interpolation for the values used for the calculation. Below the lowest and above the highest temperature the last available value for true stress and true strain is applied.

The density of the material is implemented as a constant value of $3.9 \, g/cm^3$.

---

[1]Thomas Young (13 June 1773 − 10 May 1829): British polymath and physician

True Stress	True Strain	Temperature K
701	0	573,15
754	0,001998003	573,15
916	0,004788517	573,15
512	0	1023,15
572	0,001998003	1023,15
853	0,040661982	1023,15
17,15656	0	1423,15
46,95658	0,01	1423,15
81,58749	0,02	1423,15
99,03832	0,03	1423,15
103,97428	0,04	1423,15
19,39089	0	1473,15
42,01069	0,01	1473,15
61,51762	0,02	1473,15
70,10266	0,03	1473,15
70,72623	0,04	1473,15
17,35117	0	1523,15
30,94927	0,01	1523,15
37,04914	0,02	1523,15
40,8355	0,03	1523,15
41,53312	0,04	1523,15
11,78681	0	1573,15
23,31094	0,01	1573,15
24,29106	0,02	1573,15
24,73348	0,03	1573,15
24,94081	0,04	1573,15

Table 3.2: Temperature dependent true stress and true strain

The elements used for the mechanical stress analysis have the ABAQUS label CAX4. They are linear elements with four nodes, which have the same coordinates as in the heat transfer analysis. The only load in the mechanical stress analysis is the time dependent temperature field from the heat transfer calculations. The result values are imported into the stress analysis for every time step and integration point. The option of interpolation is used to assure a correct calculation for other element types.

The results of the simulations are presented and discussed in the following chapter 4.

4 Results and Discussion

This chapter illustrates the results of the FEM-model described in the preceding chapter. For the evaluation data are generated in form of CSV-files in ABAQUS. Further analysis is performed with these data using the software MATLAB. The results are presented with regard to the coordinate axis depicted in Figure 4.2a.

4.1 Heat Transfer Analysis

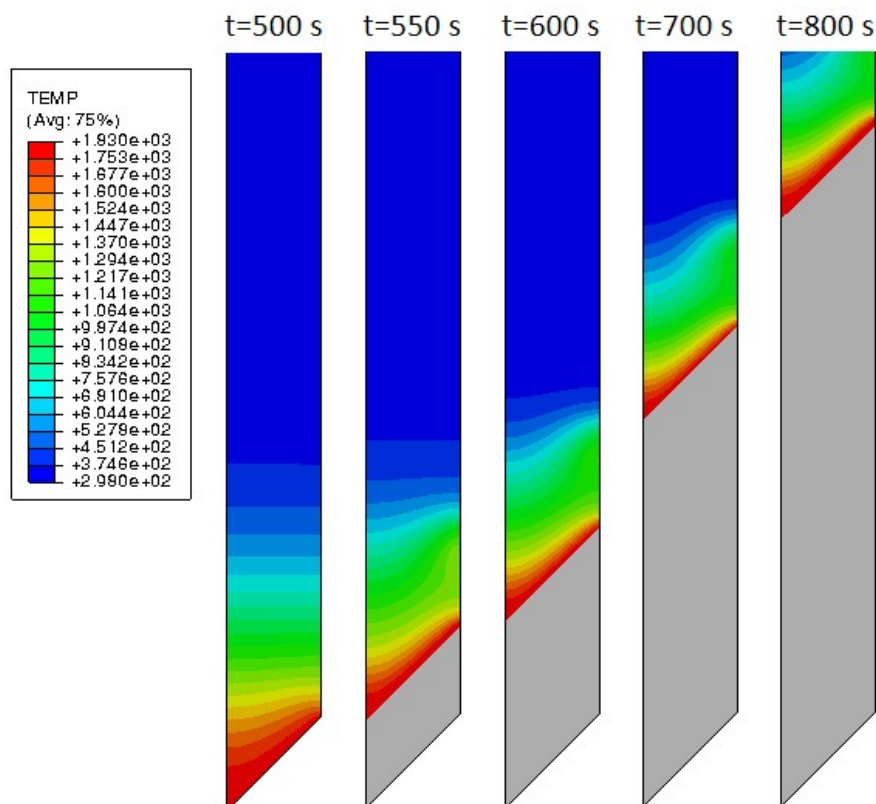### 4.1.1 Temperature Development

Figure 4.1: Evolution of the melting process represented by the temperature field. The grey area represents deactivated elements that reached the melting point.

Figure 4.1 shows the temperature development in the electrode during melting. This temperature profiles are taken at multiple points in time of the melting process. At the beginning of the melting process (t=0 s) the electrode is heated with a ramp function, that raises the temperature at the boundary within 500 s from ambient temperature to the melting point. During this step the temperature increases in the electrode leading to a temperature profile depicted at t=500 s in Figure 4.1. After this step the temperature boundary moves to the next row of elements and triggers the motion of the heat sources. The movement of the heat sources is faster than the heat conduction in the electrode. Once the moving boundary "catches up" with the initial temperature profile, the temperature profile remains stationary relative to the moving boundary (cf. Figure 4.1 t=600 s and t=700 s). The grey areas represent the melted parts of the electrode. These elements are still in the model but deactivated by setting the Young's modulus to a very low value (cf.: section 3.3).
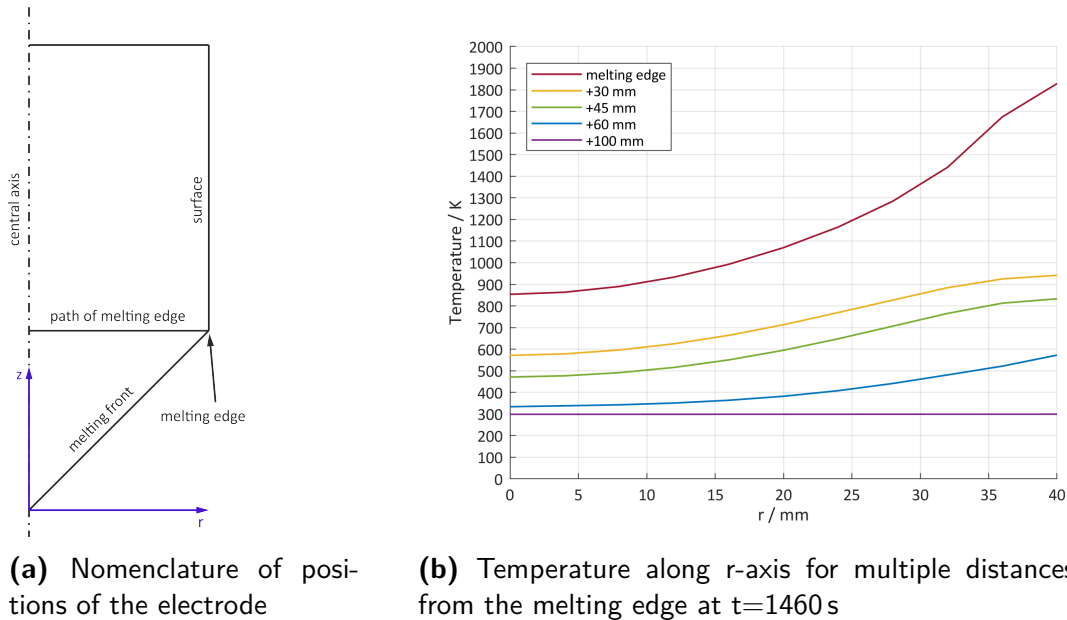

(a) Nomenclature of positions of the electrode

(b) Temperature along r-axis for multiple distances from the melting edge at t=1460 s

Figure 4.2: Temperature development during melting for multiple positions of the electrode

Figure 4.2b describes the temperature evolution along the r-axis (from the central axis to the surface) for multiple positions along the z-axis. The curve called *melting edge* shows that the elements at the surface reach the melting point at T=1832.15 K and that there is a temperature drop towards the center. The other curves show a rapid temperature drop along the z-axis. 60 mm above the melting edge the surface temperature drops under 600 K compared to the melting point of 1832.15 K. 100 mm above the melting edge the electrode is at ambient temperature along the whole r-axis.
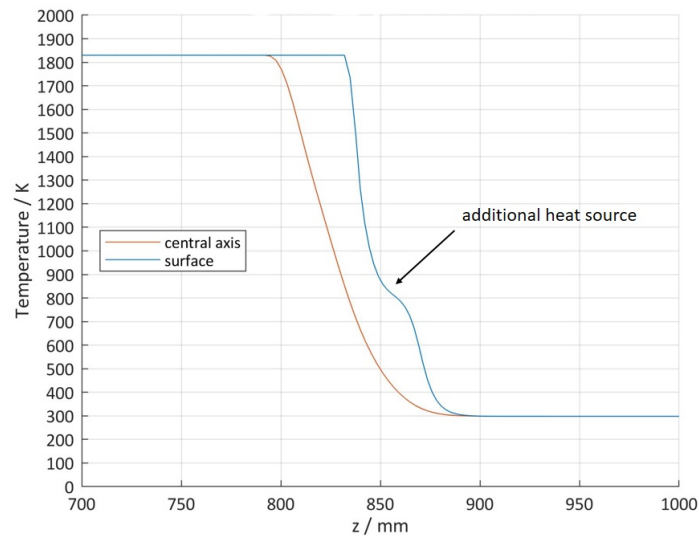
Figure 4.3: Temperature distribution along z-axis and the surface

These results show a temperature drop of over 1500 K over a distance of less than 100 mm along the electrode. The reason for this is that the movement of the heat source is faster than the heat conduction depending on the thermal conductivity λ. As described in subsection 3.2.1 this value is low compared to other metals which is the reason for the high temperature gradient in this process. Figure 4.3 presents the temperature curves along the z-axis at the end of the melting process. The melting tip is at a 45° angle and thus leads to a temperature difference between the surface and the central axis for the same position along the H-axis of the electrode. The marked position of the temperature curve at the surface shows the influence of the additional heat source.

4.1.2 Temperature Distribution with Additional Heat Sources

A second set of simulations is performed with the goal to study the potential to lower the temperature gradient along the z-axis. For this reason additional heat sources are placed along the surface representing additional induction coils. Multiple combinations of arrangements regarding the position are performed. The heat sources also exhibit various amplitudes of the applied heat flux. This represents multiple settings of electric current and applied frequencies of the actual induction coils. The nomenclature of the displayed functions using the example of the first listed name in the legend is: 2HS=number of heat sources, 08-08=representative numbers for the distance between the melting edge and the distance to the next heat source (in this case the first heat source is located 8 elements above the melting egde and the
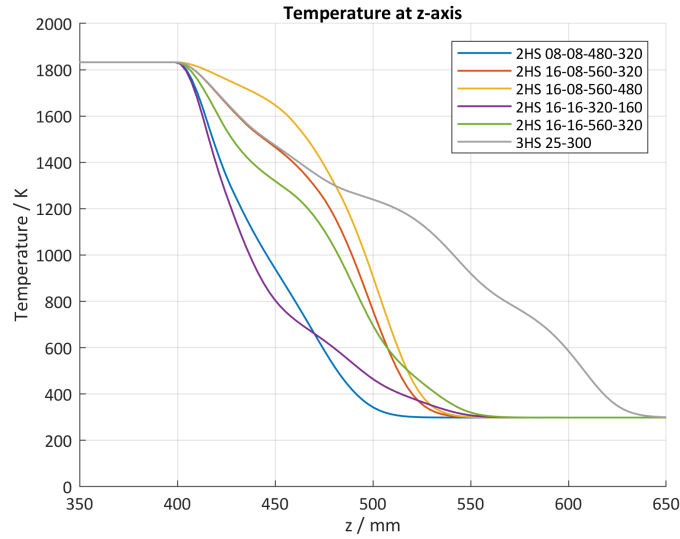
Figure 4.4: Temperature along z-axis for arrangements of multiple heat sources

second heat source is another 8 elements above the first heat source), 480-320=value of maximum heat flux respectively for both heat sources.
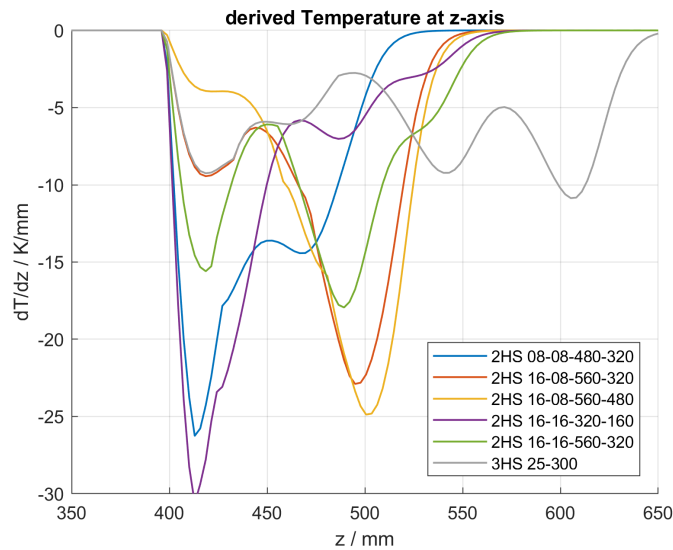

Figure 4.5: Derived temperature along z-axis for arrangements of multiple heat sources

Figure 4.4 shows the results of the temperature distribution along the z-axis for the most relevant combinations of two heat sources positioned along the electrode and an additional one with three heat sources. For a better understanding of the decrease of the temperature along this axis Figure 4.5 displays the function's derivative of the temperature with regard to the z-coordinate.

All functions show distinct maxima at multiple points. Function 2HS-16-16-320-160 reaches a maximum temperature gradient of $30\,\mathrm{K/mm}$. The function of two heat sources that performs best, regarding the temperature gradient is 2HS-16-16-560-320, showing a maximum of $18\,\mathrm{K/mm}$. With the use of three heat sources it is possible to reduce the temperature gradient to a value of $11\,\mathrm{K/mm}$. For the comparison of the corresponding stresses the reader is referred to subsection 4.2.5.

4.1.3 Temperature Distribution with Superheated Melt

As another possible influencing factor on the temperature field the superheating of the melt is analysed. For this analysis the boundary condition at the melting edge is set to $50\,\mathrm{K}$ and $100\,\mathrm{K}$ above the melting point of $1832\,\mathrm{K}$. Figure 4.6 displays the temperature distribution along the z-axis for the simulation with a boundary condition at the melting point and the two superheated variations. The increased temperature has little effect on the temperature curves. $25\,\mathrm{mm}$ above the melting edge the temperature difference in the electrode between the displayed functions reaches its minimum. Hence only $25\,\mathrm{mm}$ above the melting edge there is no detectable influence of the superheated melt in the electrode any more.
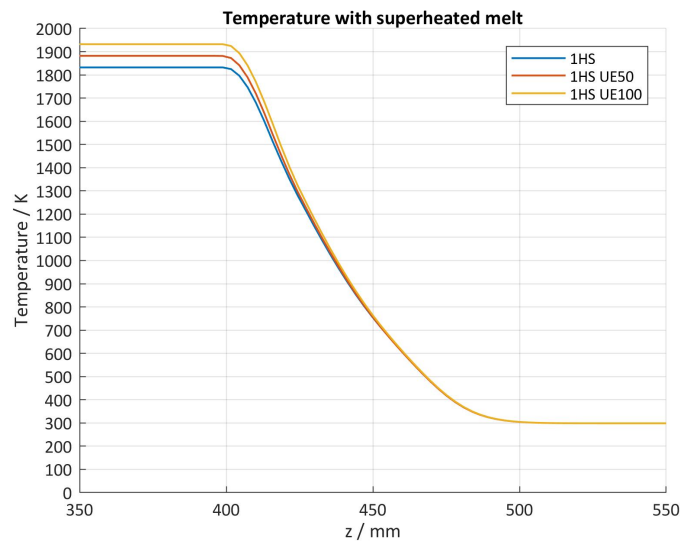

Figure 4.6: Temperature along z-axis with superheated melt for three different temperature boundary conditions: 1HS=1832.15 K, 1HS UE50=1882.15 K and 1HS UE100=1932.15 K.

4.2 Stress Analysis

The stress analysis is performed with the same procedures as the heat transfer analysis. The figures in this section depict the Mises stresses σ_{Mises} and the stresses in direction of the symmetry axis σ_z (S22 in ABAQUS) as the prevalent stresses in the electrode.
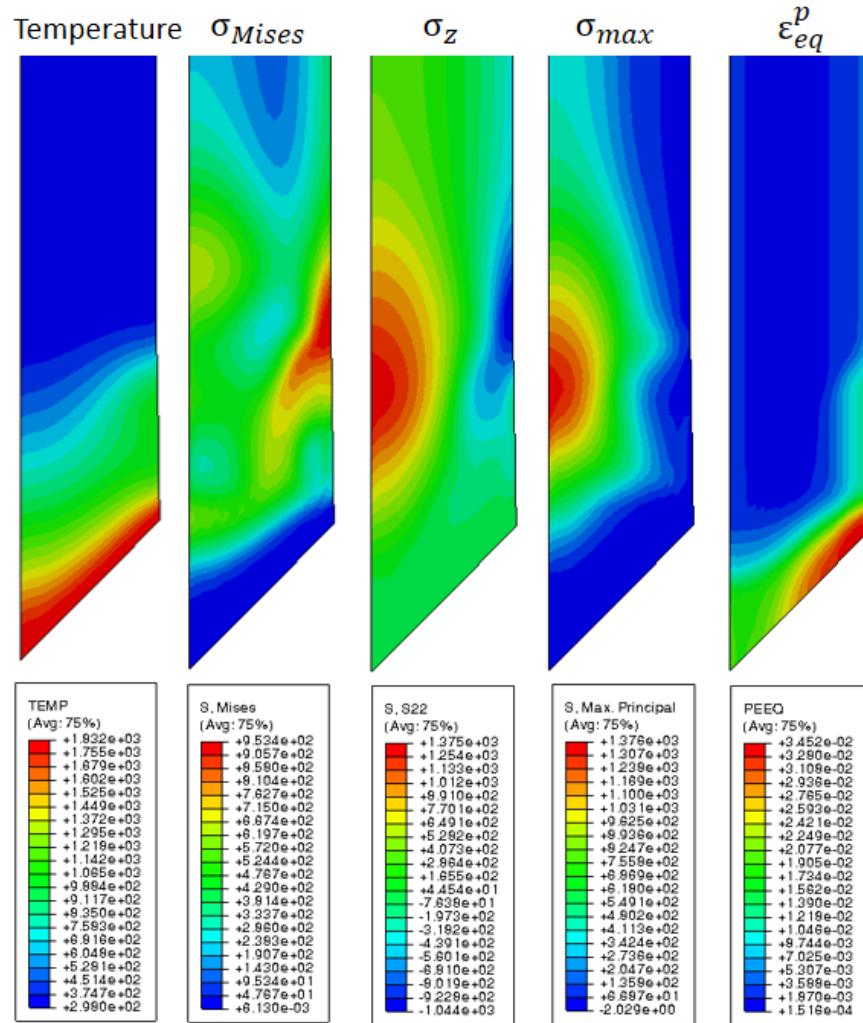

Figure 4.7: Comparison of the temperature, σ_{Mises}, σ_z, σ_{max} and ε^p_{eq} for for the melting process at t=980 s

Figure 4.7 compares three different stress conditions with the temperature and the equivalent plastic strain ε^p_{eq} (PEEQ in ABAQUS). These stresses and the strain are caused by the thermal load of the melting process.

Figure 4.8 shows the maximum principal stresses with its directions. It is evident that the predominant stress component is σ_z.
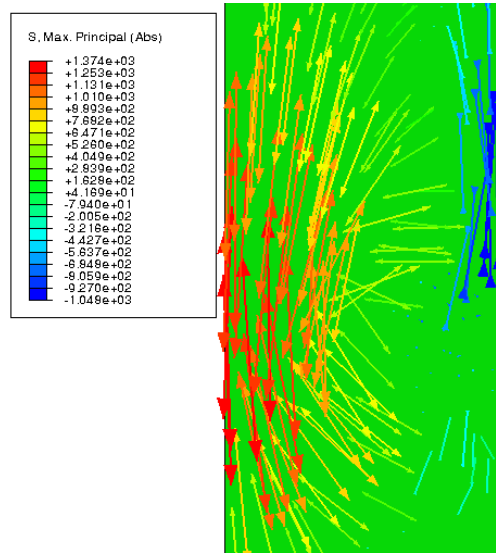
Figure 4.8: σ_{max} with its directions at t=980 s

If the stress field of σ_z is compared to the temperature field it can be shown, that the highest stress values arise in a zone with slightly increased temperature. The thermal expansion in the heated zone pulls on the central axis and compresses the surface of the electrode. Note that σ_z is significantly higher that σ_{Mises}. This is due to the fact that the stress state in the center of the electrode is highly triaxial whereas the deviatoric part, which accounts for the Mises stress, is comparably low. It is possible that due to these stresses cracks will initiate at the central axis of the electrode. These cracks will propagate towards the surface and subsequently lead to a total damage of the electrode. It is also possible that the zone with high compressive stresses at the surface could stop the crack propagation and that during the real process cracks remain undetected. To make a valid prediction for the crack development and propagation further investigations are necessary.

The highest ε_{eq}^p is located at the melting front and at the surface above. Compared to σ_z a zone with high plastic strain is located right under the zone of the highest compressive stresses at the surface of the electrode.

4.2.1 Residual Stresses After Cooling

During the cooling of the electrode a temperature difference occurs between the center and the surface. This temperature difference leads to stresses in the component. If these stresses reach the yield strength, irreversible deformations remain and thus residual stresses remain in the component, see Figure 4.9 for these residual stresses in the electrode after cooling. Figure 4.9b shows that along the central axis the stresses have positive values and hence are tensile stresses. Along the surface the values are

negative and hence compressive stresses. A short distance before the ends of the cylinder there is a stress peak, both in the center and at the surface. This peak arises because of the geometry of the electrode. At the peaks σ_z reaches maximum values of 500 MPa. Along the remaining length, σ_z has a constant value of 400 MPa.

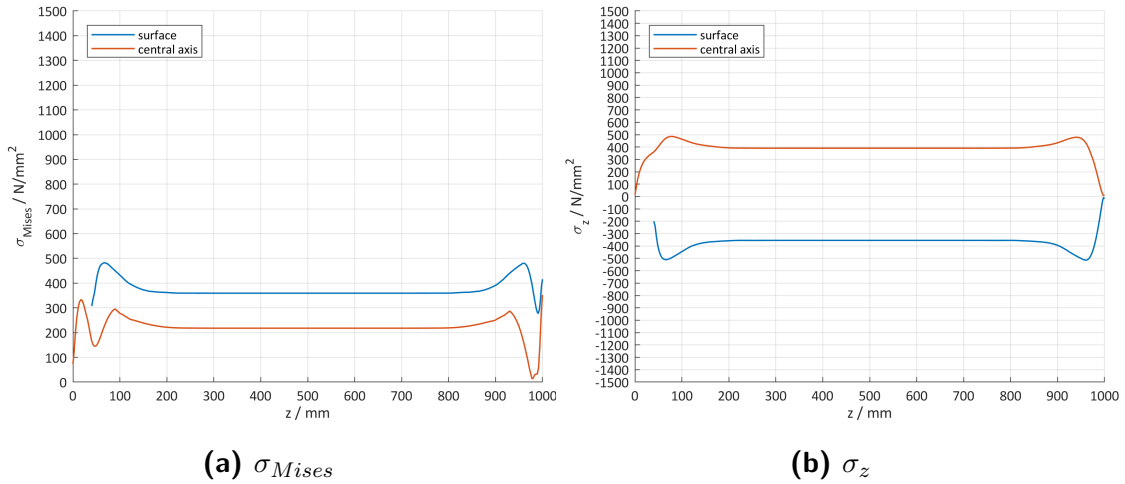**(a)** σ_{Mises} **(b)** σ_z

Figure 4.9: Residual stresses after cooling at t=0 s

4.2.2 Superimposed Stresses During Melting

Once the melting process starts, the residual stresses from the cooling process are superimposed with the stresses due to the local heating of the electrode. Figure 4.10 display the stress distribution during the melting process of the electrode, with Figures 4.10a and 4.10b at the beginning, Figures 4.10c and 4.10d in the middle and Figures 4.10e and 4.10f at the end of this process.

The local heat input raises the stresses in front of the melting edge rapidly, leading to a stress peak of 1150 MPa at the central axis shortly after the start. The stresses do not show a change of sign neither at the central axis nor at the surface, hence the resulting stresses at the central axis remain tensile and at the surface compressive.

The zone where the stress peak occurs is small compared to the dimension of the electrode, which can be traced back to the small heat-affected zone of this process. In the middle of the electrode the stress peak reaches a value of 1320 MPa. Left of this peak the stress disappears, since this part of the electrode has already melted.

Along the middle part of the electrode the stress peak remains unchanged. At the end the resulting stress due to melting is superimposed with the stress peak of the residual stresses from cooling, leading to a maximum value of 1380 MPa.
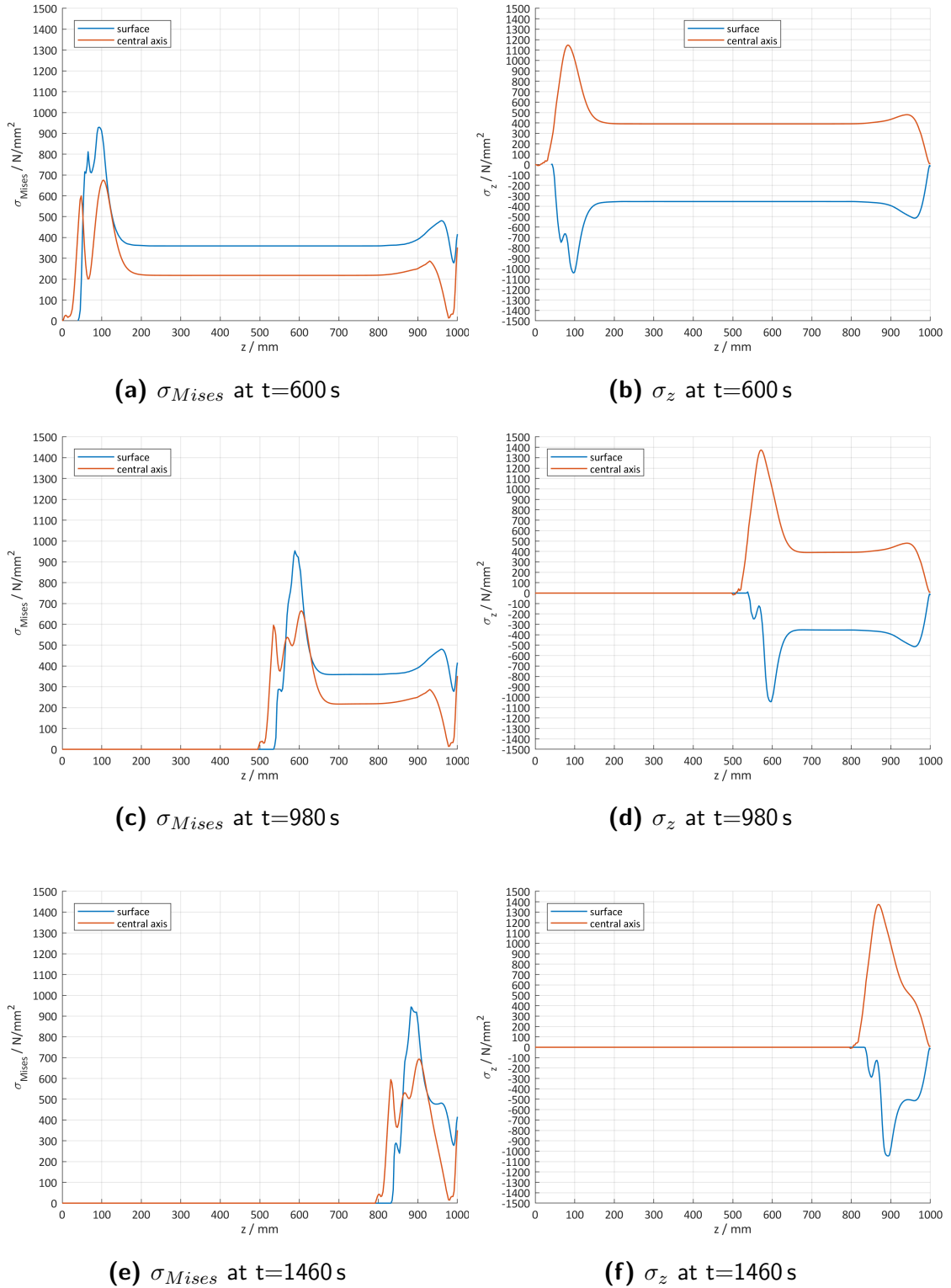
(a) σ_{Mises} at t=600 s

(b) σ_z at t=600 s

(c) σ_{Mises} at t=980 s

(d) σ_z at t=980 s

(e) σ_{Mises} at t=1460 s

(f) σ_z at t=1460 s

Figure 4.10: σ_{Mises} and σ_z at multiple points in time of the melting process. The evaluation is performed along paths at the central axis and the surface of the electrode respectively.

4.2.3 Influence of Residual Stresses on Total Stresses

To evaluate the influence of the residual stresses on the total stresses, a simulation is performed that omits the preceding cooling step for the melting process. Figure 4.11 displays a comparison of the stress distributions for the same process, the only difference being the omitted cooling step. Along the z-axis the only stresses that occur are due to the local heating of the melting process, leading to a difference of the stress value of 400 MPa in the middle of the electrode. The stress peak due to the melting process reaches a maximum value of 1120 MPa, which is approx. 250 MPa less that the peak of the process with residual stresses.
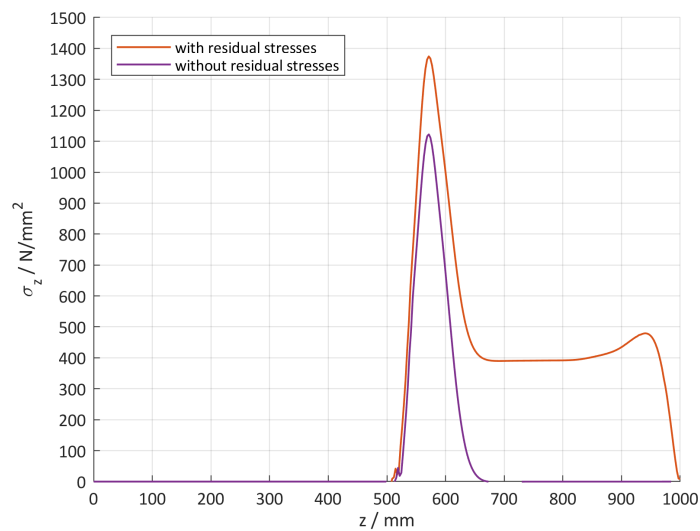

Figure 4.11: Comparison of σ_z's for the melting process for an electrode with and without residual stresses due to cooling at t=980 s

The results of this simulation show that the residual stresses for the cooling process have an influence on the total stresses during melting. The fact that the difference of the stress values at the peak is less than the difference along the rest of the electrode shows that these stresses cannot simply be added and that the residual stresses change the stress field above the melting front.

4.2.4 Comparison of Multiple Electrode Diameters

To evaluate the influence of the geometry in this process, a simulation with a smaller diameter of the electrode is performed. Figure 4.12 displays σ_z's of electrodes with diameters 40 mm and 80 mm. The general shape of the functions is the same for both diameters. The curve pertaining to D=40 mm has a stress peak that is considerably smaller compared to the larger diameter. The maximum value reaches 770 MPa. The

function also shows the influence of the residual stresses from the cooling process, which are below 200 MPa along the middle of the electrode and reach a peak of 250 MPa shortly before the end. This peak of the residual stresses is slightly closer to the end compared with the larger diameter solution.
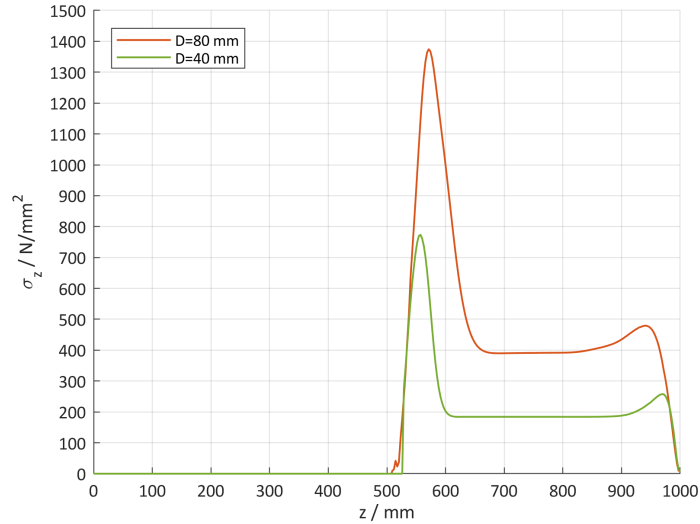

Figure 4.12: Comparison of σ_z's for diameters 40 mm and 80 mm

As displayed in Figure 4.12 the size of the electrode has a great influence on the stress distribution. For the simulation of the smaller diameter the process parameters are the same, i.e. the melting speed remains unchanged. This process would lead to only one quarter of the production volume in the same time compared to the larger diameter. A higher melting rate, that would lead to a comparable production volume has not been tested.

4.2.5 Comparison of Multiple Arrangements of Heat Sources

The evaluation of the stresses caused by heating with multiple heat sources is performed based on the results from the heat transfer analysis in subsection 4.1.2. For this reason the stresses are evaluated for the arrangements of multiple heat sources with the lowest temperature gradients, which are 2HS-16-08-560-320, 2HS-16-08-560-480, 2HS-16-16-560-320 and 3HS-25-300. The overall distribution of the stresses show a similar trend compared to the arrangement with only one heat source. The peaks of these functions are 70 MPa to 110 MPa lower compared to an arrangement of one heat source. The melting process with three heat sources leads to a peak of 1210 MPa.

These results show that the stress peak can be lowered by means of multiple heat sources, that are positioned along the surface of the electrode. These heat sources
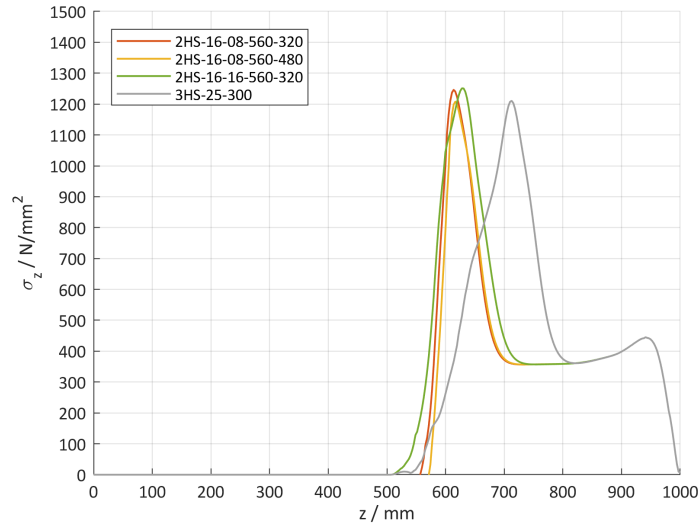
Figure 4.13: Comparison of σ_z's for multiple arrangements of heat sources

allow preheating of parts of the electrode prior to the melting process. Compared to the results in subsection 4.1.2 the temperature gradients do not have the expected influence on the stress conditions. The curve for 2HS-16-08-560-480 shows the smallest stress peak of the two heat source arrangements, but has a comparably high value of the temperature gradient (25 K/mm). The lowest temperature gradient is achieved with the arrangement of three heat sources (11 K/mm). The resulting stress peak lies in the same range compared to 2HS-16-08-560-480.

One possible explanation for this phenomenon could be that with tendency to increase the temperature at the central axis, there is also more volume that expands due to thermal expansion. This local expansion could influence the surrounding material in such a way that the stresses increase in front of the melting zone.

4.2.6 Influence of Superheating

The influence of a superheated melt on the stress conditions is depicted in Figure 4.14. The curves show σ_z for the boundary condition T_m=1832 K (melting point), and T=T_m+50 K and T=T_m+100 K. The difference of the stress peaks is minimal, although there is a trend, that with increasing temperature of the melt the resulting stress can be reduced.
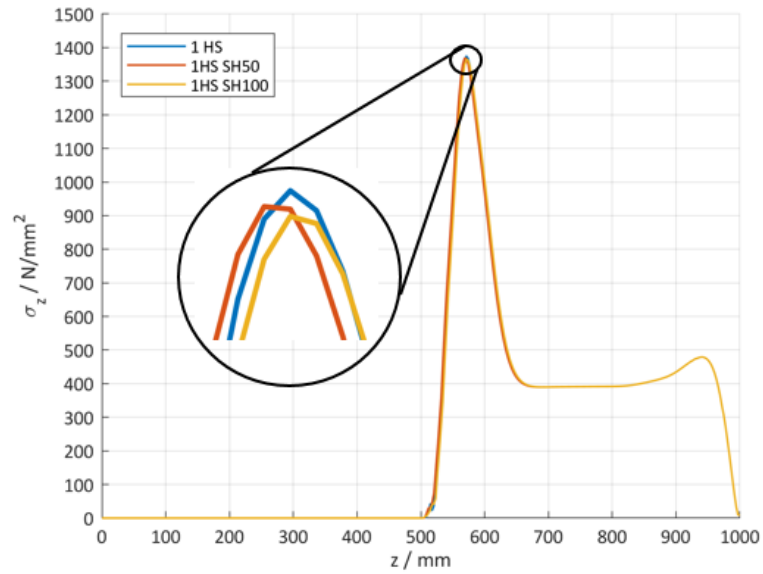
Figure 4.14: Comparison of σ_z's for superheated melt

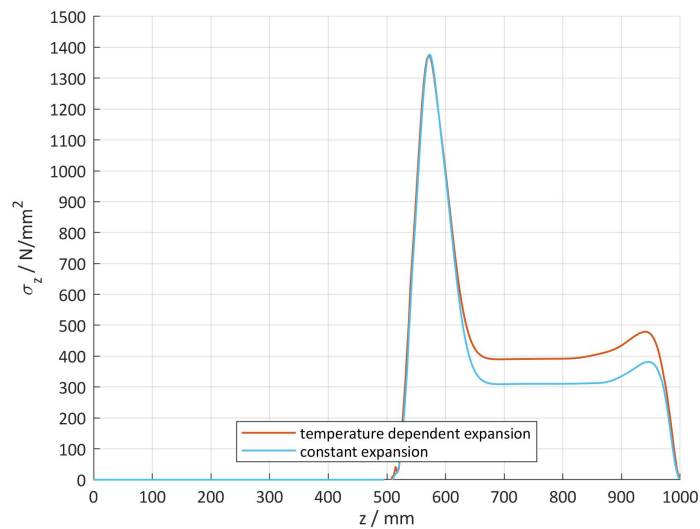## 4.2.7 Influence of Constant Thermal Expansion

Figure 4.15: Comparison of σ_z's for constant and temperature dependent thermal expansion

Achtermann et al. (2014) states that the reason for the formation of defects during a continuous melting process are phase transformations. These phase transformations occur in the range of the eutectic temperature and the transition temperature to the β single phase region (cf.: Figure 2.1). Within this range the thermal expansion coefficient increases rapidly due to the volume change of the phase transformation. To evaluate this phenomenon a simulation with a constant coefficient of thermal

expansion has been set up. The value chosen for this test is 2.86×10^{-5} K^{-1}, which leads to the same total expansion for the total temperature range of the simulation as the temperature dependent α. The other process parameters remain unchanged.

Figure 4.15 depicts σ_z along the electrode axis for the constant and for the temperature dependent coefficient of thermal expansion. The residual stresses in the middle of the electrode along the central axis are significantly reduced reaching values slightly above 300 MPa. The peak of the residual stresses also shows a slightly smaller value compared to the results of the simulation using a temperature dependent coefficient of thermal expansion. Interestingly this change does not affect the maximum stress peak above the melting front. A further analysis of this phenomenon has not been performed.

5 Conclusion and Outlook

The main goal of this thesis was to build a versatile model to simulate local heat input in the material called TNM. Using the example of the EIGA process the melting of an electrode has been simulated and the results regarding the heat transfer and the thermally induced stresses have been evaluated. The used tools allow for changes of the geometry, the method and position of heat input in the electrode, and for further changes of process parameters. Moreover such a simulation gives insight into a process, where measurements are limited.

The results discussed in chapter 4 show a comparably slow transfer of heat, which can be traced back to the microstructural properties of intermetallic TiAl-alloys. This leads to high temperature gradients during a melting process such as the EIGA-process. This unidirectionally introduced heat causes a local expansion of the component, which subsequently causes stresses. The stresses that are depicted in chapter 4 are generally too high to ensure material cohesion. This is due to a lack of material data, especially at low temperatures, but displays trends of the stress evolution that lead to a better understanding of this process. It is to be expected that electrodes processed with the used parameters will fail due to tensile stresses located at the central axis.

The use of multiple heat sources reduces the temperature gradients along the central axis of the electrode, which should reduce the thermally induced stresses. However, such a process modification also leads to more volume that expands with increasing temperature and thus generates higher stresses. It seems like these two effects cancel each other out. The tested arrangements of multiple heat sources only had a minor effect on reducing the maximum occurring stresses.

The residual stresses of the cooling process and the size of the electrode have the greatest impact on the stress evolution. From an engineering point of view it is necessary to reduce these residual stresses to a minimum to ensure a safe melting process. From an economic point of view large electrodes are preferable. However, as long as a reliable and safe production of TiAl powders cannot be ensured with large electrodes, small electrodes will prevail in an industrial environment.

Improvements for the present FEM-model could be: (i) the use of second order elements to capture stress concentrations more effectively (although these elements show a disadvantage for severe distortions), (ii) implementation of a failure criterion to display the formation of cracks due to high stresses, (iii) implementation of defects or inclusions that originate in a preceding processing step to generate a simulation that depicts the real process in an even more accurate way, (iv) implementation of a visco-elasto-plastic material behaviour to reproduce the zones of the electrode that reach temperatures close to the melting point in an improved manner, (v) calculation of the heat input by means of a thermo-electro-magnetic simulation.

A further improvement using the already existing tools is the reduction of the stress maxima by finding an ideal arrangement of multiple heat sources. A simulation is always only as reliable as the data that has been entered. For this reason it is necessary for a simulation that covers a process from ambient temperature to the melting point, to have a complete material database for every implemented material parameter. Of particular interest is the temperature range between the forging temperature and the melting point.

The use of γ-TiAl alloys for aviation, in particular TNM, with its extraordinary material properties already has an impact on the environment. In conclusion, the problems that arise during the manufacturing of components made of TNM should be investigated and solved, to further increase the usage of this lightweight material.

List of Figures

List of Tables

Bibliography

Abaqus-Documentation, U. (2018). Version 6.18. *Dassault systemes.*

Achtermann, D.-I. M., Fürwitt, W., Güther, V., and Nicolai, D.-M. H.-P. (2014). Method for the production of a β-γ-tial base alloy. US Patent 8,668,760.

Appel, F., Clemens, H., and Fischer, F. D. (2016). Modeling concepts for intermetallic titanium aluminides. *Progress in Materials Science*, 81.

Appel, F., Paul, J. D. H., and Oehring, M. (2011). *Gamma titanium aluminide alloys: science and technology.* John Wiley & Sons.

Balla, V. K., Das, M., Mohammad, A., and Al-Ahmari, A. M. (2016). Additive Manufacturing of γ-TiAl: Processing, Microstructure, and Properties. *Advanced Engineering Materials*, 18(7):1208–1215.

Blackburn, M. and Malley, D. (1993). Plasma arc melting of titanium alloys. *Materials & Design*, 14(1):19–27.

Clemens, H. and Mayer, S. (2013). Design, processing, microstructure, properties, and applications of advanced intermetallic TiAl alloys. *Advanced Engineering Materials*, 15(4):191–215.

Clemens, H. and Mayer, S. (2015). Pulvermetallurgie von intermetallischen Titanaluminiden. *BHM Berg- und Hüttenmännische Monatshefte*, 160:513–516.

Clemens, H. and Mayer, S. (2016). Intermetallic titanium aluminides in aerospace applications – processing, microstructure and properties. *Materials at High Temperatures*, 33(4-5):560–570.

Clemens, H., Mayer, S., and Heilmaier, M. (2018). Pulvermetallurgische herstellung von innovativen hochtemperaturwerkstoffen. *BHM Berg- und Hüttenmännische Monatshefte.*

Clemens, H., Wallgram, W., Kremmer, S., Güther, V., Otto, A., and Bartels, A. (2008). Design of novel β-solidifying TiAl alloys with adjustable β/B2-phase fraction and excellent hot-workability. *Advanced Engineering Materials*, 10(8):707–713.

Ebel, T., Ferri, O. M., Limberg, W., and Schimansky, F.-p. (2011). METAL INJECTION MOULDING OF ADVANCED TITANIUM ALLOYS. pages 1–13.

Gerling, R., Clemens, H., and Schimansky, F. (2004). Powder metallurgical processing of intermetallic gamma titanium aluminides. *Advanced Engineering Materials*, 6(1-2):23–38.

Güther, V., Allen, M., Klose, J., and Clemens, H. (2018). Metallurgical processing of titanium aluminides on industrial scale. *Intermetallics*, 103:12–22.

Güther, V., Otto, A., Kestler, H., and Clemens, H. (1999). Processing of gammatial based ingots and their characterization. *Gamma Titanium Aluminides*, pages 225–230.

Güther, V., Rothe, C., Winter, S., and Clemens, H. (2010). Metallurgy, Microstructure and Properties of Intermetallic TiAl Ingots. *BHM Berg- und Hüttenmännische Monatshefte*, 155(7):325–329.

Hohman, M. and Ludwig, N. (1994). System for the production of powders from metals. US Patent 5,284,329.

Lock, G. S. H. (1996). *Latent heat transfer: an introduction to fundamentals*. Number 43. Oxford University Press on Demand.

LPWtechnologies (2018). Methoden der pulverproduktion. [https://www.lpwtechnology.com/de/technical-library/powder-production/; accessed 5-March-2019].

Marek, R. and Nitsche, K. (2012). Praxis der Wärmeübertragung. *Hanser, Leipzig*.

Mayer, S., Erdely, P., Fischer, F. D., Holec, D., Kastenhuber, M., Klein, T., and Clemens, H. (2017). Intermetallic β-Solidifying γ-TiAl Based Alloys - From Fundamental Research to Application. *Advanced Engineering Materials*, 19(4):1–27.

MTU Aero Engines (2018). Geared turbofan, mtu aero engines. [https://www.mtu.de/technologies/world-class-technology/geared-turbofantm/T; accessed 5-March-2019].

Revil-Baudard, M., Jardy, A., Combeau, H., Leclerc, F., and Rebeyrolle, V. (2014). Solidification of a vacuum arc-remelted zirconium ingot. *Metallurgical and Materials Transactions B*, 45(1):51–57.

Schloffer, M. (2013). *Gefüge und Eigenschaften der intermetallischen TNM-Legierung*. PhD thesis, Montanuniversität Leoben, Franz-Josef-Str. 18, 8700 Leoben, Austria. An optional note.

Schloffer, M., Iqbal, F., Gabrisch, H., Schwaighofer, E., Schimansky, F. P., Mayer, S., Stark, A., Lippmann, T., Göken, M., Pyczak, F., and Clemens, H. (2012). Microstructure development and hardness of a powder metallurgical multi phase γ-TiAl based alloy. *Intermetallics*, 22:231–240.

Schwaighofer, E., Clemens, H., Lindemann, J., Stark, A., and Mayer, S. (2014a). Hot-working behavior of an advanced intermetallic multi-phase γ-TiAl based alloy. *Materials Science and Engineering A*, 614:297–310.

Schwaighofer, E., Clemens, H., Mayer, S., Lindemann, J., Klose, J., Smarsly, W., and Güther, V. (2014b). Microstructural design and mechanical properties of a cast and heat-treated intermetallic multi-phase γ-tial based alloy. *Intermetallics*, 44:128–140.

Stephan, H. D. B. K. (2008). Wärme und Stoffübertragung. *6. neu bearbeitete Auflage ed Springer-Verlag*.

Sun, P., Fang, Z. Z., Zhang, Y., and Xia, Y. (2017). Review of the methods for production of spherical ti and ti alloy powder. *Jom*, 69(10):1853–1860.

VDI (2013). VDI-Wärmeatlas. 11. bearbeite und erweiterte Auflage.

Wallgram, W., Schm, T., Cha, L., Das, G., Clemens, H., and Jeglitsch, F. (2009). Technology and mechanical properties of advanced c-TiAl based alloys. *Materials Research*, pages 1021–1030.

Wikipedia contributors (2018a). Ingot — Wikipedia, the free encyclopedia. [Online; accessed 12-March-2019].

Wikipedia contributors (2018b). Skin effect — Wikipedia, the free encyclopedia. [Online; accessed 5-March-2019].

A Appendix

A.1 MATLAB Code

TNM input file generator

Jakob Bialowas
00735352
Institut für Mechanik
first version: 10.09.18
latest version: 28.09.18

Contents

- Code
- Definition of variables to be passed in the calculation
- Calculation of Coordinates of nodes of melting front
- Calculation of elements and asigning nodes to the elements of melting mesh
- Calculation of remaining nodes and mesh
- Concatenation of all nodes to one matrix of nodes for electrode
- Calculation of elements and assignment of nodes to the elements of remaining mesh
- Concatenation of all elements to one matrix of elements
- Calculation of node sets for total electrode
- Calculation of element sets for total electrode
- Print results of nodes of melting front to text file
- Print results of elements of melting front to text file
- Print results of node sets of melting front and remaining nodes to text file
- Print results of all Nodes to text file
- Print results of element generation to text file

- Print Steps
- Print Input File

Code

Prepare workspace

```
close all;
clear all;
clc;
```

Definition of variables to be passed in the calculation

Variables that must be defined for the calculation: LTotal, rTotal, angle, NoElEB

```
% Geometry
LTotal=1000.0; % lenght of the electrode in mm
rTotal=10.0; % radius of the electrode in mm
angle=pi/4; % angle between the bottom egde and the cetral axis
% of the electrode in radiants

% Mesh definition
NoElEB=10.0;
% Number of elements at the bottom edge of the electrode
NoSEB=NoElEB+1;
% Number of seeds at the bottom edge of the electrode

LEB=rTotal/sin(angle);
 % lenght of the bottom edge of the electrode
LElEB=LEB/NoElEB;
% lenght of one side of an element at the bottom edge
LElEC=LElEB;
% lenght of one side of an element at the central edge

NoSEC=(LTotal-200)/LElEC;
% Number of seeds at the central edge of the electrode
NoSECInt=double(NoSEC-(NoSEC-int16(NoSEC)));
```

```
% cutting positions after decimal point
```

Calculation of Coordinates of nodes of melting front

```
NoNtotalM=NoSEB*NoSECInt;
% total number of nodes of melting front

% Preallocate entries of the array "Nodes" containing the name
%(or number) of the node and it's coordinates. First entry is
% the name, second entry is the x-coordinate, third entry is
% the y-coordinate

% for loop to asign node numbers in a systematic manner
for j=1:NoSECInt
for i=1:NoSEB
NoNodesM((j*NoSEB-NoSEB)+i)=(11100+i)+(j-1)*100;
end
end


NoNodesM=NoNodesM';

% for loop to calculate x-coordinates of nodes
for j=1:NoSECInt
for i=1:NoSEB
XNodesM((j*NoSEB-NoSEB)+i)=(i-1)*LElEB*cos(angle);
end
end


XNodesM=XNodesM';

% for loop to calculate y-coordinates of nodes
for j=1:NoSECInt
for i=1:NoSEB
YNodesM((j*NoSEB-NoSEB)+i)=(j-1)*LElEC+(i-1)*LElEB*sin(angle);
end
end


YNodesM=YNodesM';
```

```
% Merge Name, X-coordinate and Y-coordinate in one matrix for
% printing into text file
NodesM=[NoNodesM, XNodesM, YNodesM]';
```

Calculation of elements and asigning nodes to the elements of melting mesh

```
NoEltotalM=NoNtotalM-NoElEB-NoSECInt;
% total number of elements of melting front

NoElM=zeros(1,NoEltotalM);
% preallocate matrix with element numbers with zeros

% for loop to asign element numbers in a systematic manner
for j=1:(NoSECInt-1)
for i=1:NoElEB
NoElM((j*NoElEB-NoElEB)+i)=(11100+i)+(j-1)*100;
end
end

NoNodesEIN1=NoNodesM;
NoNodesEIN1(NoSEB:NoSEB:end)=[];

NoNodesEIN2=NoNodesM;
NoNodesEIN2((1+NoSEB):NoSEB:end)=[];

NoNodesEIN3=NoNodesM;
NoNodesEIN3((1+2*NoSEB):NoSEB:end)=[];

NoNodesEIN4=NoNodesM;
NoNodesEIN4(2*NoSEB:NoSEB:end)=[];

% for loops to asign nodes to elements
for i=1:NoEltotalM
ElN1M(i)=NoNodesEIN1(i);
end
```

```
for i=1:NoEltotalM
ElN2M(i)=NoNodesEIN2(i+1);
end


for i=1:NoEltotalM
ElN3M(i)=NoNodesEIN3(i+NoSEB+1);
end


for i=1:NoEltotalM
ElN4M(i)=NoNodesEIN4(i+NoSEB);
end


% concatenate matrices to one matrix of elements
ElementsM=[NoElM;ElN1M; ElN2M; ElN3M; ElN4M];
```

Calculation of remaining nodes and mesh

```
% number of remaining nodes at the symetry axis until the end
% of a 1000mm long electrode
NoNRM=double(int16((LTotal-YNodesM(length(YNodesM)-NoSEB+1))/LElEC));


% length of one element at the Y-axis for the remainig mesh
LElECRM=(LTotal-YNodesM(length(YNodesM)-NoSEB+1))/NoNRM;


% length of one element at the radiation edge for the remainig mesh
LElERRM=(LTotal-YNodesM(length(YNodesM)))/NoNRM;


% asigning node numbers to remainig mesh
NoNodesRM=zeros(NoNRM,1);
for j=1:NoNRM
for i=1:NoSEB
NoNodesRM((j*NoSEB-NoSEB)+i)=
=(NoNodesM(length(NoNodesM)-NoSEB+1)+99+i)+(j-1)*100;
end
end


% calculation of x-coordinates of remainig mesh
```

```
for j=1:NoNRM
for i=1:NoSEB
XNodesRM((j*NoSEB-NoSEB)+i)=(i-1)*LElEB*cos(angle);
end
end

XNodesRM=XNodesRM';

% calculation of y-coordinates of remainig mesh
for j=1:NoNRM
for i=1:NoSEB
Y2RM=YNodesM(length(YNodesM))+LElERRM*j;
Y1RM=YNodesM(length(YNodesM)-NoSEB+1)+LElECRM*j;
deltaY=Y2RM-Y1RM;
deltaX=rTotal;
angleBeta=atan(deltaY/deltaX);
LEi=sqrt(deltaX^2+deltaY^2)/(NoSEB-1);
YNodesRM((j*NoSEB-NoSEB)+i)=YNodesM(length(YNodesM)-NoSEB+1)+
+j*LElECRM+(i-1)*LEi*sin(angleBeta);
end
end

YNodesRM=YNodesRM';

% concatination of node numbers and coordinates into one
% matrix of melting front
NodesRM=[NoNodesRM, XNodesRM, YNodesRM]';

% calculation of matrix length
NoNtotalRM=length(NoNodesRM);
```

Concatenation of all nodes to one matrix of nodes for electrode

```
NodesTotal=[NodesM,NodesRM];
NoNodesTotal=[NoNodesM;NoNodesRM];
NNodesTotal=length(NoNodesTotal);
XNodesTotal=[XNodesM;XNodesRM];
```

```
YNodesTotal=[YNodesM;YNodesRM];

% plot(XNodesTotal,YNodesTotal,'.');
```

Calculation of elements and assignment of nodes to the elements of remaining mesh

```
NoEltotalRM=NoNtotalRM-NoNRM;

NoElRM=zeros(1,NoEltotalRM);

for j=1:(NoNRM)
for i=1:NoElEB
NoElRM((j*NoElEB-NoElEB)+i)=NoNodesM(length(NoNodesM)-
-NoSEB+1)+(i-1)+(j-1)*100;
end
end

NoNodesInter=NoNodesM((length(NoNodesM)-NoSEB+1):1:end);
NoNodesEIN1RM=[NoNodesInter;NoNodesRM];
NoNodesEIN1RM(NoSEB:NoSEB:end)=[];

NoNodesEIN2RM=[NoNodesInter;NoNodesRM];
NoNodesEIN2RM((1+NoSEB):NoSEB:end)=[];

NoNodesEIN3RM=[NoNodesInter;NoNodesRM];
NoNodesEIN3RM((1+2*NoSEB):NoSEB:end)=[];

NoNodesEIN4RM=[NoNodesInter;NoNodesRM];
NoNodesEIN4RM(2*NoSEB:NoSEB:end)=[];

for i=1:NoEltotalRM
ElN1RM(i)=NoNodesEIN1RM(i);
end

for i=1:NoEltotalRM
ElN2RM(i)=NoNodesEIN2RM(i+1);
```

```
end

for i=1:NoEltotalRM
ElN3RM(i)=NoNodesEIN3RM(i+NoSEB+1);
end

for i=1:NoEltotalRM
ElN4RM(i)=NoNodesEIN4RM(i+NoSEB);
end

ElementsRM=[NoElRM; ElN1RM; ElN2RM; ElN3RM; ElN4RM];
```

Concatenation of all elements to one matrix of elements

```
ElementsTotal=[ElementsM, ElementsRM];
NoElTotal=[NoElM,NoElRM];
```

Calculation of node sets for total electrode

```
NoNsetsIL=16; % maximum number of nodes in one line of node sets

% Nodeset of axis symmetry on Y-axis
NsetYASym=NoNodesTotal(1:NoSEB:end);
NsetYASymNL=mod(length(NsetYASym),NoNsetsIL);

% dividing into two matrices for printing not fully filled lines
NsetYASym16=NsetYASym(1:1:(length(NsetYASym)-NsetYASymNL));
NsetYASymMod=NsetYASym((length(NsetYASym)-NsetYASymNL+1):1:end);

% Nodeset of radiation edge
NsetRadER=NoNodesTotal(NoSEB:NoSEB:end);
NsetRadET=NoNodesTotal((length(NoNodesTotal)-NoSEB+1):1:end);
NsetRadE=[NsetRadER;NsetRadET];

% dividing into two matrices for printing not fully filled lines
NsetRadENL=mod(length(NsetRadE),NoNsetsIL);
NsetRadE16=NsetRadE(1:1:(length(NsetRadE)-NsetRadENL));
NsetRadEMod=NsetRadE((length(NsetRadE)-NsetRadENL+1):1:end);
```

```
% Nodeset Encastre
NsetEncastre=NoNodesTotal(length(NoNodesTotal)-NoSEB+1);
```

Calculation of element sets for total electrode

```
ElSetRadER=NoElTotal((2*NoElEB):NoElEB:end);
ElSetRadET=NoElTotal((length(NoElTotal)-NoElEB+1):1:end);
ElSetRadE=[ElSetRadER,ElSetRadET];
ElSetRadEB=NoElTotal(1:1:NoElEB);


ElSetRadENL=mod(length(ElSetRadE),NoNsetsIL);
ElSetRadE16=ElSetRadE(1:1:(length(ElSetRadE)-ElSetRadENL));
ElSetRadEMod=ElSetRadE((length(ElSetRadE)-ElSetRadENL+1):1:end);


ElSetRadERNL=mod(length(ElSetRadER),NoNsetsIL);
ElSetRadER16=ElSetRadER(1:1:(length(ElSetRadER)-ElSetRadERNL));
ElSetRadERMod=ElSetRadER((length(ElSetRadER)-ElSetRadERNL+1):1:end);


ElSetRadETNL=mod(length(ElSetRadET),NoNsetsIL);
ElSetRadET16=ElSetRadET(1:1:(length(ElSetRadET)-ElSetRadETNL));
ElSetRadETMod=ElSetRadET((length(ElSetRadET)-ElSetRadETNL+1):1:end);


ElSetRadEBNL=mod(length(ElSetRadEB),NoNsetsIL);
ElSetRadEB16=ElSetRadEB(1:1:(length(ElSetRadEB)-ElSetRadEBNL));
ElSetRadEBMod=ElSetRadEB((length(ElSetRadEB)-ElSetRadEBNL+1):1:end);
```

Print results of nodes of melting front to text file

```
formatSpecNodesM = '%10.0f, %10.5f, %10.5f\n';


fileNodesM = fopen('NodesM.txt','w');
fprintf(fileNodesM,'%6s\n','*Node');
fprintf(fileNodesM,formatSpecNodesM,NodesM);
fclose(fileNodesM);
```

Print results of elements of melting front to text file

```
formatSpecElementsM = '%5.0f, %5.0f, %5.0f, %5.0f, %5.0f\n';


fileElementsM = fopen('ElementsM.txt','w');
fprintf(fileElementsM,'%20s\n','*Element, type=DCAX4');
fprintf(fileElementsM,formatSpecElementsM,ElementsM);
fclose(fileElementsM);
```

Print results of node sets of melting front and remaining nodes to text file

```
% Generate format for fprintf for nodesets of the melting front


NsetMF=NoNodesM((NoSEB-NoSEB+1):(NoSEB));


if length(NsetMF)<=16
NsetMFNL=mod(length(NsetMF),NoNsetsIL);
formatSpecNodesetMF16='%5.0f\n';


for i=1:(NsetMFNL-1)
formatSpecNodesetMF16=strcat('%5.0f, ', formatSpecNodesetMF16);
end
end


if length(NsetMF)>16
formatSpecNodesetMF16='%5.0f\n';
for i=1:(NoNsetsIL-1)
formatSpecNodesetMF16=strcat('%5.0f, ', formatSpecNodesetMF16);
end
end
% Generate format for fprintf for nodesets of boundary conditions


% Y-Axis Symmetry
formatSpecNodesetsBYAS16='%5.0f, ';


for i=1:(NoNsetsIL-2)
```

```
formatSpecNodesetsBYAS16=strcat(formatSpecNodesetsBYAS16,'%5.0f, ');
end
formatSpecNodesetsBYAS16=strcat(formatSpecNodesetsBYAS16,'%5.0f\n');


formatSpecNodesetsBYASMod='%5.0f\n';


for i=1:(NsetYASymNL-1)
formatSpecNodesetsBYASMod=strcat('%5.0f, ', formatSpecNodesetsBYASMod);
end


% Radiation Edge
formatSpecNodesetsBRE16='%5.0f, ';


for i=1:(NoNsetsIL-2)
formatSpecNodesetsBRE16=strcat(formatSpecNodesetsBRE16,'%5.0f, ');
end
formatSpecNodesetsBRE16=strcat(formatSpecNodesetsBRE16,'%5.0f\n');


formatSpecNodesetsBREMod='%5.0f\n';


for i=1:(NsetRadENL-1)
formatSpecNodesetsBREMod=strcat('%5.0f, ', formatSpecNodesetsBREMod);
end


% Generate format for Elementsets
% Radiation element set


formatSpecElsetsE16='%5.0f,    ';


for i=1:(NoNsetsIL-2)
formatSpecElsetsE16=strcat(formatSpecElsetsE16,'%5.0f,    ');
end
formatSpecElsetsE16=strcat(formatSpecElsetsE16,'%5.0f\n');


formatSpecElsetsEMod='%5.0f\n';
for i=1:(ElSetRadENL-1)
formatSpecElsetsEMod=strcat('%5.0f,    ', formatSpecElsetsEMod);
end
```

```
formatSpecElsetRadER16='%5.0f,     ';

for i=1:(NoNsetsIL-2)
formatSpecElsetRadER16=strcat(formatSpecElsetRadER16,'%5.0f,     ');
end
formatSpecElsetRadER16=strcat(formatSpecElsetRadER16,'%5.0f\n');

formatSpecElsetRadERMod='%5.0f\n';
for i=1:(ElSetRadERNL-1)
formatSpecElsetRadERMod=strcat('%5.0f,     ', formatSpecElsetRadERMod);
end

formatSpecElsetRadET16='%5.0f,     ';

for i=1:(NoNsetsIL-2)
formatSpecElsetRadET16=strcat(formatSpecElsetRadET16,'%5.0f,     ');
end
formatSpecElsetRadET16=strcat(formatSpecElsetRadET16,'%5.0f\n');

formatSpecElsetRadETMod='%5.0f\n';
for i=1:(ElSetRadETNL-1)
formatSpecElsetRadETMod=strcat('%5.0f,     ', formatSpecElsetRadETMod);
end

formatSpecElsetRadEB16='%5.0f,     ';

for i=1:(NoNsetsIL-2)
formatSpecElsetRadEB16=strcat(formatSpecElsetRadEB16,'%5.0f,     ');
end
formatSpecElsetRadEB16=strcat(formatSpecElsetRadEB16,'%5.0f\n');

formatSpecElsetRadEBMod='%5.0f\n';
for i=1:(ElSetRadETNL-1)
formatSpecElsetRadEBMod=strcat('%5.0f,     ', formatSpecElsetRadEBMod);
end

% Print general nodesets and element sets
```

```
fileNodesets = fopen('Nodesets.txt','w');


% Print nodesets for boundary conditions
fprintf(fileNodesets, '*Nset, nset=Set-YASYMM\n');
fprintf(fileNodesets,formatSpecNodesetsBYAS16,NsetYASym16);
fprintf(fileNodesets,formatSpecNodesetsBYASMod,NsetYASymMod);


fprintf(fileNodesets, '*Nset, nset=Set-Encastre\n');
fprintf(fileNodesets, '%5.0f\n', NsetEncastre);


fprintf(fileNodesets, '*Nset, nset=Set-RadiationEdge\n');
fprintf(fileNodesets,formatSpecNodesetsBRE16,NsetRadE16);
fprintf(fileNodesets,formatSpecNodesetsBREMod,NsetRadEMod);


% Loop for nodesets of the melting front


if NoSEB<=NoNsetsIL
for i=1:NoSECInt
fprintf(fileNodesets, '*Nset, nset=n%d\n',i);
NsetiMF16=NoNodesM((NoSEB*i-NoSEB+1):(NoSEB*i));
fprintf(fileNodesets, formatSpecNodesetMF16, NsetiMF16);
end
end


if NoSEB>NoNsetsIL
for i=1:NoSECInt
fprintf(fileNodesets, '*Nset, nset=n%d\n',i);
NsetiMF=NoNodesM((NoSEB*i-NoSEB+1):(NoSEB*i));
NsetiMFNL=mod(length(NsetiMF),NoNsetsIL);
NsetiMF16=NsetiMF(1:1:(length(NsetiMF)-NsetiMFNL));
NsetiMFMod=NsetiMF((length(NsetiMF)-NsetiMFNL+1):1:end);


formatSpecNodesetiMFMod='%5.0f\n';
for i=1:(NsetiMFNL-1)
formatSpecNodesetiMFMod=strcat('%5.0f, ', formatSpecNodesetiMFMod);
end


fprintf(fileNodesets, formatSpecNodesetMF16, NsetiMF16);
```

```
fprintf(fileNodesets, formatSpecNodesetiMFMod, NsetiMFMod);


end
end

fclose(fileNodesets);

fileElementsets = fopen('Elementsets22.txt','w');

fprintf(fileElementsets, '*Elset, elset=ElSetRadE\n');
fprintf(fileElementsets,formatSpecElsetsE16,ElSetRadE16);
fprintf(fileElementsets,formatSpecElsetsEMod,ElSetRadEMod);

fprintf(fileElementsets, '*Elset, elset=ElSetRadER\n');
fprintf(fileElementsets,formatSpecElsetRadER16,ElSetRadER16);
fprintf(fileElementsets,formatSpecElsetRadERMod,ElSetRadERMod);

fprintf(fileElementsets, '*Elset, elset=ElSetRadET\n');
fprintf(fileElementsets,formatSpecElsetRadET16,ElSetRadET16);
fprintf(fileElementsets,formatSpecElsetRadETMod,ElSetRadETMod);

fprintf(fileElementsets, '*Elset, elset=ElSetRadEB\n');
fprintf(fileElementsets,formatSpecElsetRadEB16,ElSetRadEB16);
fprintf(fileElementsets,formatSpecElsetRadEBMod,ElSetRadEBMod);

fclose(fileElementsets);
```

Print results of all nodes to text file

```
formatSpecNodes = '%5.0f, %9.4f, %9.4f\n';


fileNodes = fopen('Nodes.txt','w');
fprintf(fileNodes,'%20s\n','*Node, nset=nSet-all');
fprintf(fileNodes,formatSpecNodes,NodesTotal);
fclose(fileNodes);
```

Print results of element generation to text file

```
formatSpecElements = '%5.0f,%5.0f,%5.0f,%5.0f,%5.0f\n';


fileElements = fopen('Elements.txt','w');
fprintf(fileElements,'%35s\n','*Element, elset=elSet-all, type=DCAX4');
fprintf(fileElements,formatSpecElements,ElementsTotal);
fclose(fileElements);
```

Print Steps

```
% Definition of step parameters for first step
% (heating up to melting Temp)
NoIncS1=1000;


% Definition of step parameters for heat transfer
initialTSS1=0.1;
minTSS1=0.0001;
totalTS1=1000.0;
maxTSS1=1.0;


stepParameterS1=[initialTSS1,totalTS1,minTSS1,maxTSS1];


initialTS=0.1;
minTS=0.0001;
totalT=1.69704;
maxTS=1.0;


stepParameter=[initialTS,totalT,minTS,maxTS];


formatSpecStepHT='%5.5f,%5.5f,%5.5f,%5.5f\n';


% Definition of step parameters
NoDOF=11;
% number of degree of freedom, 11 is for Temperatur
meltingTemp=1830.15;
% magnitude of Temperatur for boundary condition
```

```
% Printing first Step
fileSteps = fopen('Steps22.txt','w');
fprintf(fileSteps,'*Step, name=Step-1s, nlgeom=NO, inc=1000,
amp=ramp\n');
fprintf(fileSteps,'*Heat Transfer, end=PERIOD, deltmx=4.\n');
fprintf(fileSteps,'%d, %d, %d, %d\n', stepParameterS1);
fprintf(fileSteps,'*BOUNDARY\n');
fprintf(fileSteps,'n1, %d, %d, %d\n',NoDOF,NoDOF, meltingTemp);
fprintf(fileSteps,'** INTERACTION\n');
fprintf(fileSteps,'*SRadiate\n');
fprintf(fileSteps,'Surf-ER, R, 25., 0.9\n');
fprintf(fileSteps,'*SRadiate\n');
fprintf(fileSteps,'Surf-ET, R, 25., 0.9\n');
fprintf(fileSteps,'*Sfilm\n');
fprintf(fileSteps,'Surf-ER, F, 25., 0.028\n');
fprintf(fileSteps,'*Sfilm\n');
fprintf(fileSteps,'Surf-ET, F, 25., 0.028\n');
fprintf(fileSteps,'*Output, field, variable=PRESELECT\n');
fprintf(fileSteps,'*End Step\n');
fprintf(fileSteps,'**\n');


for i=2:NoSECInt

fprintf(fileSteps,'*Step, name=Step-%ds, nlgeom=NO, inc=1000,
amp=ramp\n',i);
fprintf(fileSteps,'*Heat Transfer, end=PERIOD, deltmx=4.\n');
fprintf(fileSteps,'%d, %d, %d, %d\n', stepParameter);
fprintf(fileSteps,'*BOUNDARY\n');
fprintf(fileSteps,'n%d, %d, %d, %d\n',i,NoDOF,NoDOF, meltingTemp);
fprintf(fileSteps,'** INTERACTION\n');
fprintf(fileSteps,'*SRadiate\n');
fprintf(fileSteps,'Surf-ER, R, 25., 0.9\n');
fprintf(fileSteps,'*SRadiate\n');
fprintf(fileSteps,'Surf-ET, R, 25., 0.9\n');
fprintf(fileSteps,'*Sfilm\n');
fprintf(fileSteps,'Surf-ER, F, 25., 0.028\n');
fprintf(fileSteps,'*Sfilm\n');
fprintf(fileSteps,'Surf-ET, F, 25., 0.028\n');
```

```
fprintf(fileSteps,'*Output, field, variable=PRESELECT\n');
fprintf(fileSteps,'*End Step\n');
fprintf(fileSteps,'**\n');


end


fclose(fileSteps);
```

Print Input File

```
fileINP = fopen('INPRadius10.txt','w');


% Print Header for inputfile
fprintf(fileINP,'*Heading
\n**
\n** JBJBJBJBJBJBJBJBJBJBJBJBJB
\n**
\n** Job name: Job-IFG-TNM-001\
n** Generated by: Abaqus/CAE 6.14-2
\n*Preprint, echo=NO, model=NO, history=NO, contact=NO
\n**\n');


% Print Nodes for inputfile
fprintf(fileNodes,'%20s\n','*Node, nset=nSet-all');
fprintf(fileNodes,formatSpecNodes,NodesTotal);


% Print Elements for Inputfile
fprintf(fileElements,'%35s\n','*Element, elset=elSet-all,
type=DCAX4');
fprintf(fileElements,formatSpecElements,ElementsTotal);


% Print Nodesets for Inputfile
fprintf(fileINP, '*Nset, nset=Set-YASYMM\n');
fprintf(fileINP,formatSpecNodesetsBYAS16,NsetYASym16);
fprintf(fileINP,formatSpecNodesetsBYASMod,NsetYASymMod);


fprintf(fileINP, '*Nset, nset=Set-Encastre\n');
fprintf(fileINP, '%5.0f\n', NsetEncastre);
```

```
fprintf(fileINP, '*Nset, nset=Set-RadiationEdge\n');
fprintf(fileINP,formatSpecNodesetsBRE16,NsetRadE16);
fprintf(fileINP,formatSpecNodesetsBREMod,NsetRadEMod);


if NoSEB<=NoNsetsIL
for i=1:NoSECInt
fprintf(fileINP, '*Nset, nset=n%d\n',i);
NsetiMF16=NoNodesM((NoSEB*i-NoSEB+1):(NoSEB*i));
fprintf(fileINP, formatSpecNodesetMF16, NsetiMF16);
end
end


if NoSEB>NoNsetsIL
for i=1:NoSECInt
fprintf(fileINP, '*Nset, nset=n%d\n',i);
NsetiMF=NoNodesM((NoSEB*i-NoSEB+1):(NoSEB*i));
NsetiMFNL=mod(length(NsetiMF),NoNsetsIL);
NsetiMF16=NsetiMF(1:1:(length(NsetiMF)-NsetiMFNL));
NsetiMFMod=NsetiMF((length(NsetiMF)-NsetiMFNL+1):1:end);


formatSpecNodesetiMFMod='%5.0f\n';
for i=1:(NsetiMFNL-1)
formatSpecNodesetiMFMod=strcat('%5.0f,    ',
formatSpecNodesetiMFMod);
end


fprintf(fileINP, formatSpecNodesetMF16, NsetiMF16);
fprintf(fileINP, formatSpecNodesetiMFMod, NsetiMFMod);


end
end


fprintf(fileINP, '*Elset, elset=ElSetRadE\n');
fprintf(fileINP,formatSpecElsetsE16,ElSetRadE16);
fprintf(fileINP,formatSpecElsetsEMod,ElSetRadEMod);


fprintf(fileINP, '*Elset, elset=ElSetRadER\n');
```

```
fprintf(fileINP,formatSpecElsetRadER16,ElSetRadER16);
fprintf(fileINP,formatSpecElsetRadERMod,ElSetRadERMod);


fprintf(fileINP, '*Elset, elset=ElSetRadET\n');
fprintf(fileINP,formatSpecElsetRadET16,ElSetRadET16);
fprintf(fileINP,formatSpecElsetRadETMod,ElSetRadETMod);


fprintf(fileINP, '*Elset, elset=ElSetRadEB\n');
fprintf(fileINP,formatSpecElsetRadEB16,ElSetRadEB16);
fprintf(fileINP,formatSpecElsetRadEBMod,ElSetRadEBMod);


% Printing first Step

fprintf(fileINP,'*Step, name=Step-1s, nlgeom=NO, inc=1000,
amp=ramp\n');
fprintf(fileINP,'*Heat Transfer, end=PERIOD, deltmx=4.\n');
fprintf(fileINP,'%d, %d, %d, %d\n', stepParameterS1);
fprintf(fileSteps,'*BOUNDARY\n');
fprintf(fileSteps,'n1, %d, %d, %d\n',NoDOF,NoDOF, meltingTemp);
fprintf(fileINP,'** INTERACTION\n');
fprintf(fileINP,'*SRadiate\n');
fprintf(fileINP,'Surf-ER, R, 298.15, 0.1\n');
fprintf(fileINP,'Surf-ET, R, 298.15, 0.1\n');
fprintf(fileINP,'*Sfilm\n');
fprintf(fileINP,'Surf-ER, F, 298.15, sfilm_cylinderwall_heating\n');
fprintf(fileINP,'Surf-ET, F, 298.15, sfilm_cylindertop_heating\n');
fprintf(fileINP,'*DFLUX\n');
fprintf(fileINP,'elset-all, BFNU,0\n');
fprintf(fileINP,'*Output, field, frequency=5\n');
fprintf(fileINP,'*Node output\n');
fprintf(fileINP,'NT, RFL\n');
fprintf(fileINP,'*Element output, direction=YES\n');
fprintf(fileINP,'HFL, TEMP\n');
fprintf(fileINP,'*Output, history, frequency=0\n');
fprintf(fileINP,'*Output, field, variable=PRESELECT, frequency=5\n');
fprintf(fileINP,'*End Step\n');
fprintf(fileINP,'**\n');
```

```
for i=2:NoSECInt

fprintf(fileINP,'*Step, name=Step-%ds, nlgeom=NO, inc=1000,
amp=ramp\n',i);
fprintf(fileINP,'*Heat Transfer, end=PERIOD, deltmx=4.\n');
fprintf(fileINP,'%d, %d, %d, %d\n', stepParameter);
fprintf(fileSteps,'*BOUNDARY\n');
fprintf(fileSteps,'n%d, %d, %d, %d\n',i,NoDOF,NoDOF, meltingTemp);
fprintf(fileINP,'** INTERACTION\n');
fprintf(fileINP,'*SRadiate\n');
fprintf(fileINP,'Surf-ER, R, 298.15, 0.1\n');
fprintf(fileINP,'Surf-ET, R, 298.15, 0.1\n');
fprintf(fileINP,'*Sfilm\n');
fprintf(fileINP,'Surf-ER, F, 298.15, sfilm_cylinderwall_heating\n');
fprintf(fileINP,'Surf-ET, F, 298.15, sfilm_cylindertop_heating\n');
fprintf(fileINP,'*DFLUX\n');
fprintf(fileINP,'elset-all, BFNU,0\n');
fprintf(fileINP,'*Output, field, frequency=5\n');
fprintf(fileINP,'*Node output\n');
fprintf(fileINP,'NT, RFL\n');
fprintf(fileINP,'*Element output, direction=YES\n');
fprintf(fileINP,'HFL, TEMP\n');
fprintf(fileINP,'*Output, history, frequency=0\n');
fprintf(fileINP,'*Output, field, variable=PRESELECT, frequency=5\n');
fprintf(fileINP,'*End Step\n');
fprintf(fileINP,'**\n');

end

fclose(fileINP);
```

A.2 Fortran Code

DFLUX User Subroutine

```fortran
c2345678901234567890123456789012345678901234567890123456789012345678901234567890
c
SUBROUTINE DFLUX(FLUX,SOL,KSTEP,KINC,TIME,NOEL,NPT,COORDS,
1 JLTYP,TEMP,PRESS,SNAME)
C
INCLUDE 'ABA_PARAM.INC'
C
DIMENSION FLUX(2), TIME(2), COORDS(3)
CHARACTER*80 SNAME

C     Defining variables for calculations
R=40.
H=10.
vMelting=50./60.
STEPTIME=3.39408
C       CHARACTER*80 pfile
C       pfile='/home/jakob/Desktop/del.txt'
C
C     Values of exponential function calculated in MATLAB
C       a=2.371E-8
C       b=0.4971
C       c=2.371E-8
a=3.512E-4
b=0.1989
c=3.512E-4
C
C     Asigning X and Y coordinates to new variables
X=COORDS(1)
Y=COORDS(2)

C     Calculation of current Y-position of heat source
YPOSITIONSTART=R
YPOSITION=R+vMElting*((KSTEP+16)*STEPTIME)
YPOSITION2=R+vMElting*((KSTEP+32)*STEPTIME)
C           YPOSITION3=R+vMElting*((KSTEP+60)*STEPTIME)

C     Values of max heat of heat flux function
Q1=560
Q2=480

C     Asigning value of heat flux to specified area with
C     expfunction calculated in MATLAB
IF(KSTEP.EQ.2)THEN
IF((Y.GE.YPOSITION).AND.(Y.LE.(YPOSITION+H)).AND.
U    ((X.LE.R).AND.(X.GE.0)))THEN

FLUX(1)=((a*exp(b*X)-c)*(exp(-(Y-YPOSITIONSTART)**2*0.005)))*Q1


ELSEIF((Y.LT.YPOSITION).AND.(Y.GE.(YPOSITION-H)).AND.
U        ((X.LE.R).AND.(X.GE.0)))THEN

FLUX(1)=((a*exp(b*X)-c)*(exp(-(Y-YPOSITIONSTART)**2*0.005)))*Q1
```

```fortran
      ELSEIF((Y.GE.YPOSITION2).AND.(Y.LE.(YPOSITION2+H)).AND.
     U    ((X.LE.R).AND.(X.GE.0)))THEN

      FLUX(1)=((a*exp(b*X)-c)*(exp(-(Y-YPOSITIONSTART)**2*0.005)))*Q2


      ELSEIF((Y.LT.YPOSITION2).AND.(Y.GE.(YPOSITION2-H)).AND.
     U        ((X.LE.R).AND.(X.GE.0)))THEN

      FLUX(1)=((a*exp(b*X)-c)*(exp(-(Y-YPOSITIONSTART)**2*0.005)))*Q2


      ELSE
      FLUX(1)=0

      ENDIF

      ENDIF


      IF(KSTEP.GT.2)THEN

      IF((Y.GE.YPOSITION).AND.(Y.LE.(YPOSITION+H)).AND.
     U      ((X.LE.R).AND.(X.GE.0)))THEN
      FLUX(1)=((a*exp(b*X)-c)*(exp(-(Y-YPOSITION)**2*0.005)))*Q1

      ELSEIF((Y.LT.YPOSITION).AND.(Y.GE.(YPOSITION-H)).AND.
     U        ((X.LE.R).AND.(X.GE.0)))THEN

      FLUX(1)=((a*exp(b*X)-c)*(exp(-(Y-YPOSITION)**2*0.005)))*Q1

      ELSEIF((Y.GE.YPOSITION2).AND.(Y.LE.(YPOSITION2+H)).AND.
     U      ((X.LE.R).AND.(X.GE.0)))THEN

      FLUX(1)=((a*exp(b*X)-c)*(exp(-(Y-YPOSITION2)**2*0.005)))*Q2

      ELSEIF((Y.LT.YPOSITION2).AND.(Y.GE.(YPOSITION2-H)).AND.
     U      ((X.LE.R).AND.(X.GE.0)))THEN

      FLUX(1)=((a*exp(b*X)-c)*(exp(-(Y-YPOSITION2)**2*0.005)))*Q2

      ELSE
      FLUX(1)=0

      ENDIF


      ENDIF

      RETURN
      END
```

A.3 Convection Calculation for Cylindrical Ingot

CONVECTION

	specific gas constant Rm	absolute zero	gravity acceleration	pressure	temperature in K
		diameter of cylinder m 0,08000	heigh of cylinder m 1,00000		
Symbols/ Formulas			g		
Unit	$\dfrac{J}{kg*K}$	C	$\dfrac{m}{s^2}$	Pa	K
	287,05800	-273,15000	9,81000	100000	273,15000
	287,05800	-273,15000	9,81000	100000	298,15000
	287,05800	-273,15000	9,81000	100000	348,15000
	287,05800	-273,15000	9,81000	100000	448,15000
	287,05800	-273,15000	9,81000	100000	548,15000
	287,05800	-273,15000	9,81000	100000	648,15000
	287,05800	-273,15000	9,81000	100000	748,15000
	287,05800	-273,15000	9,81000	100000	848,15000
	287,05800	-273,15000	9,81000	100000	948,15000
	287,05800	-273,15000	9,81000	100000	1048,15000
	287,05800	-273,15000	9,81000	100000	1148,15000
	287,05800	-273,15000	9,81000	100000	1248,15000
	287,05800	-273,15000	9,81000	100000	1348,15000
	287,05800	-273,15000	9,81000	100000	1448,15000
	287,05800	-273,15000	9,81000	100000	1548,15000
	287,05800	-273,15000	9,81000	100000	1648,15000
	287,05800	-273,15000	9,81000	100000	1748,15000
	287,05800	-273,15000	9,81000	100000	1848,15000

temperatur in °C	reference temperature for material constants	density of air $\rho = \dfrac{p}{R_S T}$	dynamic viscosity η	dynamic viscosity η
C	C	$\dfrac{kg}{m^3}$	$10^{-6}\dfrac{kg}{m*s}$	$\dfrac{kg}{m*s}$
0,00000	12,50000	1,21954019	17,8200	1,7820E-05
25,00000	25,00000	1,168410717	18,4500	1,8450E-05
75,00000	50,00000	1,078018428	19,6575	1,9657E-05
175,00000	100,00000	0,933570026	21,9291	2,1929E-05
275,00000	150,00000	0,823258077	24,0710	2,4071E-05
375,00000	200,00000	0,736260499	26,0992	2,6099E-05
475,00000	250,00000	0,665892488	28,0282	2,8028E-05
575,00000	300,00000	0,607801893	29,8711	2,9871E-05
675,00000	350,00000	0,559033387	31,6399	3,1640E-05
775,00000	400,00000	0,517509701	33,3449	3,3345E-05
875,00000	450,00000	0,481728072	34,9954	3,4995E-05
975,00000	500,00000	0,450574475	36,5992	3,6599E-05
1075,00000	550,00000	0,423205558	38,1627	3,8163E-05
1175,00000	600,00000	0,398971145	39,6909	3,9691E-05
1275,00000	650,00000	0,377361919	41,1878	4,1188E-05
1375,00000	700,00000	0,357973237	42,6556	4,2656E-05
1475,00000	750,00000	0,340479553	44,0954	4,4095E-05
1575,00000	800,00000	0,324615995	45,5069	4,5507E-05

kinematic viscosity	kinematic viscosity	isobaric coefficient of expansion	isobaric coefficient of expansion
$\upsilon = \dfrac{\eta}{\rho}$	$\upsilon = \dfrac{\eta}{\rho}$	β	β
$\dfrac{m^2}{s}$	$\dfrac{mm^2}{s}$	$10^{-3} * K^{-1}$	K^{-1}
1,5555E-05	1,5555E+01	3,5125	3,5125E-03
1,5790E-05	1,5790E+01	3,3640	3,3640E-03
1,8235E-05	1,8235E+01	3,1012	3,1012E-03
2,3489E-05	2,3489E+01	2,6835	2,6835E-03
2,9239E-05	2,9239E+01	2,3653	2,3653E-03
3,5448E-05	3,5448E+01	2,1148	2,1148E-03
4,2091E-05	4,2091E+01	1,9123	1,9123E-03
4,9146E-05	4,9146E+01	1,7453	1,7453E-03
5,6597E-05	5,6597E+01	1,6052	1,6052E-03
6,4433E-05	6,4433E+01	1,4859	1,4859E-03
7,2646E-05	7,2646E+01	1,3831	1,3831E-03
8,1228E-05	8,1228E+01	1,2937	1,2937E-03
9,0175E-05	9,0175E+01	1,2151	1,2151E-03
9,9483E-05	9,9483E+01	1,1455	1,1455E-03
1,0915E-04	1,0915E+02	1,0835	1,0835E-03
1,1916E-04	1,1916E+02	1,0278	1,0278E-03
1,2951E-04	1,2951E+02	0,9776	9,7759E-04
1,4019E-04	1,4019E+02	0,9321	9,3206E-04

thermal conductivity	thermal conductivity	specific heat capacity	specific heat capacity	thermal diffusivity
λ	λ	c_p	c_p	$a = \dfrac{\lambda}{\rho * c}$
$\dfrac{mW}{m\,K}$	$\dfrac{W}{m\,K}$	$\dfrac{kJ}{kg\,K}$	$\dfrac{J}{kg\,K}$	$\dfrac{m^2}{s}$
25,31	2,5308E-02	1,006	1006	2,0628E-05
26,25	2,6245E-02	1,0065	1006,5	2,2317E-05
28,08	2,8080E-02	1,008	1008	2,5841E-05
31,62	3,1620E-02	1,011	1011	3,3501E-05
35,00	3,5000E-02	1,0175	1017,5	4,1783E-05
38,25	3,8250E-02	1,025	1025	5,0685E-05
41,38	4,1380E-02	1,035	1035	6,0041E-05
44,42	4,4420E-02	1,045	1045	6,9936E-05
47,37	4,7370E-02	1,057	1057	8,0166E-05
50,24	5,0240E-02	1,069	1069	9,0814E-05
53,05	5,3050E-02	1,081	1081	1,0187E-04
55,80	5,5800E-02	1,093	1093	1,1330E-04
58,49	5,8490E-02	1,104	1104	1,2519E-04
61,14	6,1140E-02	1,115	1115	1,3744E-04
63,74	6,3740E-02	1,126	1126	1,5001E-04
66,31	6,6310E-02	1,136	1136	1,6306E-04
68,85	6,8850E-02	1,146	1146	1,7645E-04
71,35	7,1350E-02	1,154	1154	1,9047E-04

Prandtl-number		Rayleigh-number	Nusselt- number for vertical plate
Pr	$f_1(Pr) = \left[1 + \left(\dfrac{0.492}{Pr}\right)^{\frac{9}{16}}\right]^{\frac{-16}{9}}$	$R_{aL} = \dfrac{g\beta\Delta TL^3}{a\nu}$	$Nu_{Platte} = \left\{0.825 + 0.387[Ra * f_1(Pr)]^{\frac{1}{6}}\right\}^2$
0,7092	0,346854959	2,6847E+09	166,8878617
0,7140	0,347916407	0,0000E+00	0,680625
0,7045	0,345831395	3,2282E+09	176,6154225
0,7004	0,344924067	5,0180E+09	202,6273911
0,6984	0,344479811	4,7484E+09	199,0644809
0,6981	0,344413079	4,0414E+09	189,2392609
0,6993	0,344679861	3,3405E+09	178,3283505
0,7016	0,345190097	2,7398E+09	167,6965343
0,7046	0,345853468	2,2559E+09	157,9318951
0,7080	0,346602359	1,8683E+09	149,0359578
0,7117	0,347413817	1,5584E+09	140,9771182
0,7154	0,348221648	1,3100E+09	133,6876372
0,7190	0,34900419	1,1087E+09	127,0542207
0,7224	0,349740155	9,4515E+08	121,0263072
0,7225	0,349761756	8,1146E+08	115,4742407
0,7284	0,351031634	7,0055E+08	110,4954604
0,7310	0,351588413	6,0850E+08	105,8721465
0,7332	0,352058193	5,3078E+08	101,5733588

Nusselt- number cylinder	heat transfer coefficient vertical cylinder vertical surface	heat transfer coefficient vertical cylinder vertical surface	Prandtl-number
$Nu = Nu_{Platte} + 0{,}435\dfrac{h}{D}$	$\alpha = \dfrac{Nu * \lambda}{L}$	$\alpha = \dfrac{Nu * \lambda}{L}$	Pr
	$\dfrac{W}{m^2\ K}$	$\dfrac{mW}{mm^2\ K}$	
172,3253617	4,3611E+00	4,3611E-03	0,7092
6,118125	1,6057E-01	1,6057E-04	0,7140
182,0529225	5,1120E+00	5,1120E-03	0,7045
208,0648911	6,5790E+00	6,5790E-03	0,7004
204,5019809	7,1576E+00	7,1576E-03	0,6984
194,6767609	7,4464E+00	7,4464E-03	0,6981
183,7658505	7,6042E+00	7,6042E-03	0,6993
173,1340343	7,6906E+00	7,6906E-03	0,7016
163,3693951	7,7388E+00	7,7388E-03	0,7046
154,4734578	7,7607E+00	7,7607E-03	0,7080
146,4146182	7,7673E+00	7,7673E-03	0,7117
139,1251372	7,7632E+00	7,7632E-03	0,7154
132,4917207	7,7494E+00	7,7494E-03	0,7190
126,4638072	7,7320E+00	7,7320E-03	0,7224
120,9117407	7,7069E+00	7,7069E-03	0,7225
115,9329604	7,6875E+00	7,6875E-03	0,7284
111,3096465	7,6637E+00	7,6637E-03	0,7310
107,0108588	7,6352E+00	7,6352E-03	0,7332

characteristic length of vertical cylinder horizontal surface 0,02	$l_{char} = \dfrac{d}{4}$		

$f_2(Pr) = \left[1 + \left(\dfrac{0.322}{Pr}\right)^{\frac{11}{20}}\right]^{\frac{-20}{11}}$	Rayleigh-number $Ra_L = \dfrac{g\beta\Delta T L^3}{a\nu}$	Nusselt- number horizontal plate $Nu_{Platte} = 0.766[Ra * f_2(Pr)]^{\frac{1}{5}}$
0,403317338	2,6847E+09	49,10640997
0,404398218	0,0000E+00	0
0,402274481	3,2282E+09	50,92421168
0,401349595	5,0180E+09	55,59545866
0,400896586	4,7484E+09	54,97241327
0,40082853	4,0414E+09	53,22640317
0,401100591	3,3405E+09	51,2437941
0,401620819	2,7398E+09	49,26464818
0,402296976	2,2559E+09	47,40250343
0,403060027	1,8683E+09	45,66596493
0,4038865	1,5584E+09	44,0571416
0,404708938	1,3100E+09	42,57051647
0,40550531	1,1087E+09	41,18986594
0,406253992	9,4515E+08	39,91062983
0,406275961	8,1146E+08	38,71206614
0,407567111	7,0055E+08	37,61458226
0,408132955	6,0850E+08	36,57983924
0,40861026	5,3078E+08	35,60196559

heat transfer coefficient horizontal plate top surface	heat transfer coefficient horizontal plate top surface	characteristic length horizontal cylinder horizontal surface 0,125663706	Nusselt- number horizontal cylinder horizontal surface
$\alpha = \dfrac{Nu * \lambda}{L}$	$\alpha = \dfrac{Nu * \lambda}{L}$	$f_3(Pr) = \left[1 + \left(\dfrac{0.559}{Pr}\right)^{\frac{9}{16}}\right]^{\frac{-16}{9}}$	$Nu_{Platte} = \left\{0.752 + 0.387[Ra * f_3(Pr)]^{\frac{1}{6}}\right\}^{2}$
$\dfrac{W}{m^2\,K}$	$\dfrac{mW}{mm^2\,K}$		
6,2138E+01	6,2138E-02	0,327168512	162,0097937
0,0000E+00	0,0000E+00	0,328209577	0,565504
7,1498E+01	7,1498E-02	0,32616479	171,4956165
8,7896E+01	8,7896E-02	0,325275204	196,8767453
9,6202E+01	9,6202E-02	0,324839689	193,3958829
1,0180E+02	1,0180E-01	0,324774273	183,8059779
1,0602E+02	1,0602E-01	0,325035799	173,1599741
1,0942E+02	1,0942E-01	0,325536018	162,7890987
1,1227E+02	1,1227E-01	0,326186433	153,2663138
1,1471E+02	1,1471E-01	0,326920791	144,5923959
1,1686E+02	1,1686E-01	0,327716614	136,7361217
1,1877E+02	1,1877E-01	0,328508993	129,6308733
1,2046E+02	1,2046E-01	0,329276678	123,165905
1,2201E+02	1,2201E-01	0,329998766	117,291698
1,2338E+02	1,2338E-01	0,330019961	111,8791047
1,2471E+02	1,2471E-01	0,331266124	107,0307851
1,2593E+02	1,2593E-01	0,331812594	102,5265809
1,2701E+02	1,2701E-01	0,332273717	98,33877827

heat transfer coefficient horizontal cylinder horizontal surface	heat transfer coefficient horizontal cylinder horizontal surface	heat transfer coefficient vertikale plate	heat transfer coefficient vertikale plate
$\alpha = \dfrac{Nu * \lambda}{L}$	$\alpha = \dfrac{Nu * \lambda}{L}$	$\alpha = \dfrac{Nu * \lambda}{L}$	$\alpha = \dfrac{Nu * \lambda}{L}$
$\dfrac{W}{m^2\ K}$	$\dfrac{mW}{mm^2\ K}$	$\dfrac{W}{m^2\ K}$	$\dfrac{mW}{mm^2\ K}$
3,2627E+01	3,2627E-02	5,2794E+01	5,2794E-02
1,1811E-01	1,1811E-04	2,2329E-01	2,2329E-04
3,8321E+01	3,8321E-02	6,1992E+01	6,1992E-02
4,9539E+01	4,9539E-02	8,0088E+01	8,0088E-02
5,3865E+01	5,3865E-02	8,7091E+01	8,7091E-02
5,5948E+01	5,5948E-02	9,0480E+01	9,0480E-02
5,7020E+01	5,7020E-02	9,2240E+01	9,2240E-02
5,7543E+01	5,7543E-02	9,3114E+01	9,3114E-02
5,7775E+01	5,7775E-02	9,3515E+01	9,3515E-02
5,7808E+01	5,7808E-02	9,3595E+01	9,3595E-02
5,7724E+01	5,7724E-02	9,3485E+01	9,3485E-02
5,7562E+01	5,7562E-02	9,3247E+01	9,3247E-02
5,7327E+01	5,7327E-02	9,2893E+01	9,2893E-02
5,7067E+01	5,7067E-02	9,2494E+01	9,2494E-02
5,6748E+01	5,6748E-02	9,2004E+01	9,2004E-02
5,6478E+01	5,6478E-02	9,1587E+01	9,1587E-02
5,6173E+01	5,6173E-02	9,1116E+01	9,1116E-02
5,5835E+01	5,5835E-02	9,0591E+01	9,0591E-02